VIC-Glacier (VIC-GL)

Model Set-up and Deployment for the Peace, Fraser, and Columbia

---

VIC Generation 2 Deployment Report

Volume 6

Markus Schnorbus

Pacific Climate Impacts Consortium

University of Victoria

Victoria, BC

11 March 2020

Citation

Schnorbus, M.A., 2020: *VIC Glacier (VIC-GL) – Model Set-up and Deployment for the Peace, Fraser, and Columbia*, VIC Generation 2 Deployment Report, Volume 6, Pacific Climate Impacts Consortium, University of Victoria, Victoria, BC, 73 pp.

About PCIC

The Pacific Climate Impacts Consortium is a regional climate service centre at the University of Victoria that provides practical information on the physical impacts of climate variability and change in the Pacific and Yukon Region of Canada. PCIC operates in collaboration with climate researchers and regional stakeholders on projects driven by user needs. For more information see http://pacificclimate.org.

Disclaimer

Acknowledgement

I gratefully acknowledge the financial support of BC Hydro.

Table of Contents

List of Figures

List of Tables

1 Background

The hydro-climatology of British Columbia (BC) is complex, in part due to its proximity to the Pacific Ocean, mountainous terrain and large latitudinal expanse. Historical changes to climate and hydrology have been documented in British Columbia and western North America by Rodenhuis et al. (2009) and changes in extremes have been discussed by Peterson et al. (2013). Historical changes are in part attributable to climate variability on annual to decadal timescales, such as teleconnection patterns coming from El Niño/Southern Oscillation (ENSO) or the Pacific Decadal Oscillation (PDO). In addition, recent hydro-climatic trends in western North America have also been affected by anthropogenic climate change, predominantly in the form of increased regional warming (Barnett et al. 2008; Bonfils et al. 2008; Pierce et al. 2008). The regional response to climate variability and trends can potentially affect all aspects of the hydrologic cycle, including the hydrologic extremes of flood and drought (Hamlet and Lettenmaier 2007; Sheffield and Wood 2008; Dai 2013; Hirabayashi et al. 2013). Ultimately it is recognized that the hydro-climatic system can no longer be considered stationary, and from a management perspective the past may become progressively less informative of future conditions (Milly et al. 2008).

Consequently, the aim of the hydrologic Impacts (HI) Theme at the Pacific Climate Impacts Consortium (PCIC) is to quantify the effects of climate change and variability on water resources within the Pacific and Yukon region (PYR) of western Canada. All this is to be accomplished at spatial scales relevant to regional and local management and over multiple planning and adaptation timeframes. Of particular interest for management and planning is a greater emphasis on knowledge regarding changes in hydrologic variability and changes in extremes, such as flood and drought, and phenomena that affect that variability, such as changes in the frequency and intensity of storms affecting the PYR.

This report describes the deployment of the VIC-GL model, which was used to produce hydrologic projections utilizing climate experiments from the Coupled Model Intercomparison Project Phase 5 (CMIP5; Taylor et al. 2012), which are based on the new Representative Concentration Pathways (RCP) emissions scenarios (Moss et al. 2010; van Vuuren et al. 2011). These projections cover the full range of potential future climates encompassed by the various RCP scenarios, but with greater emphasis on RCP4.5 and RCP8.5. Projections are based on improved hydrologic modelling, with more explicit emphasis on accurately modelling potential cryospheric changes within the PYR.

The purpose of this report is to describe the deployment of the VIC-GL model as employed to produce the CMIP5-based hydrologic projections that are available via the PCIC data portal. Currently these projections are only available in the Peace, Fraser and Columbia basins, and this report will focus on model deployment within this domain. This report will provide a brief description of the VIC-GL model, including parametrization of land cover, soil, topography, and the surface drainage network (Section 2), the model calibration process (Section 3), model verification (Section 4), and the experimental design used to produce the hydrologic projection ensembles (Section 5).

2 VIC-GL Model

2.1 Model Description

Hydrologic projections were produced using an upgraded version of the Variable Infiltration Capacity (VIC) hydrology mode (Schnorbus 2018). VIC is a spatially distributed macro-scale hydrologic model that calculates water and energy balances in a grid cell, with sub-grid variability of the soil column, land surface vegetation classes and topography represented statistically. The model computes the water fluxes for a range of hydrologic processes such as evapotranspiration, snow accumulation, snowmelt, infiltration, soil moisture and surface and subsurface runoffs. The present version uses three-soil layers to represent soil moisture processes. The model uses variable infiltration curves to represent the spatial heterogeneity of runoff generation and uses the Arno conceptual model (Todini 1996) for subsurface flow generation. Surface runoff from the upper two soil layers is generated when the moisture exceeds the storage capacity of the soil. Spatial variability is modelled by sub-diving the model domain into a computational grid with a spatial resolution of 0.0625°. Sub-grid variability is described using hydrologic response units (HRUs), which are derived using vegetation classes and 200-m elevation bands. The model runs at a 3-hour temporal resolution, but output is aggregated to a daily resolution. The fluxes from the model are collected and routed downstream using an offline routing model called RVIC, which is based on the method described in Lohmann et al. (1998). Detailed description of the VIC model is available in Liang et al. (1994, 1996) and Cherkauer et al. (2003). The VIC model has seen extensive application in the study of climate change impacts in British Columbia (e.g. Shrestha et al. 2012; Schnorbus et al. 2014; Werner et al. 2013; Shrestha et al. 2016; Islam et al. 2017; Curry et al. 2019).

For many catchments, glaciers provide water to streams, especially during summer and early autumn when seasonal snowpacks have been depleted. Increased emissions of greenhouse gasses will accelerate warming in the decades ahead leading to strong mass loss and subsequent retreat of alpine glaciers. Therefore, to simulate more accurately the response of the cryospheric components of the basin, we have produced and upgraded version of the VIC model, called VIC-GL, that explicitly models glacier mass balance (accumulation, melt and runoff) and glacier dynamics (change in glacier area).

The VIC-GL model is not designed to allow lateral communication between cells; hence, it can’t be used to directly model hydrologic or cryospheric features that occupy more than a single cell (such as large lakes or ice fields), or that flow from one cell into another cell (such as valley glaciers). Consequently, glacier dynamics is simulated by coupling VIC-GL to the UBC Regional Glaciation Model (RGM). The RGM model is described in detail by Jarosch et al. (2013) and Clarke et al. (2015). In the coupled system, glacier surface mass balance estimated with the VIC-GL model is converted to a high-resolution 100-m equal-area grid. This gridded mass balance field is then used to force the RGM model, the output of which is updated surface topography that reflects changes in the spatial distribution of glacier thickness. VIC-GL is subsequently updated with the new glacier areas. Coupling takes place on an annual basis and occurs at the end of the water year (30 September). RGM requires an estimate of the bed (or sub-glacial) topography, and we use the results from Clarke et al. (2013). Glacier thickness at the end of each water year is calculated as the difference between the updated surface topography and static bed topography. The description of the new glacier surface mass and energy balance routines in VIC-GL is described in Schnorbus (2018).

2.2 Model Parameterization

2.2.1 Land Cover

Parameterization of vegetation characteristics in the VIC-GL model is based on discretizing the land surface into various vegetation classes. The vegetation classes are used to capture the relevant spatial variation in vegetation properties by dividing the continuum of land cover types into discrete classes, where each discrete class can be considered homogeneous with respect to a description of its properties (e.g., height, leaf area index, etc.). Ultimately, land cover classification is a trade-off between capturing existing spatial variability while maintaining a manageable number of vegetation classes. We employed the North America Land Cover dataset, edition 2 (Natural Resources Canada/ The Canada Centre for Mapping and Earth Observation (NRCan/CCMEO) et al. 2013) produced as part of the North America Land Change Monitoring System (NALCMS). The NALCMS land cover data set divides North America into 19 land cover classes representing c. 2005 conditions.

In the original landcover classification the *Temperate or sub-polar needleleaf forest* is too homogeneous, as it does not reflect know spatial variation in the needleleaf forest class within British Columbia due to changes in elevation and differences between coastal and interior forests. Consequently, this land cover class was further subdivided using an unsupervised classification scheme based on the iterative self-organizing (ISO) clustering algorithm and maximum likelihood classification (using the Multivariate toolbox in ArcGIS). Classification was based on vegetation height (h) and leaf area index (L). Leaf are index data is from the GEOV1 global time series dataset (Baret et al. 2013; Camacho et al. 2013). Vegetation height is based on global mapping using spaceborne light detection and ranging (lidar) (Simard et al. 2011). The final NA land cover classification, with needleleaf forest further sub-divided, contains 22 land cover classes (Table 1; Figure 1). Although an Ice class already exists in the NALCMS-based land cover inventory, the extent and location of glaciers and ice fields was updated using the more complete data of the Randolph Glacier Inventory (RGI; Pfeffer et al. 2014), version 3.2, which was released September 2013. Landcover and vegetation parameterization is discussed in greater detail in Schnorbus (2016).

2.2.2 Soil

Soil classification and parameterization were based primarily on physical soil data from the Soils Program in the Global Soil Data Products CD-ROM (Global Soil Data Task 2014). The soil data contained in the Soils Program are from a global pedon database produced by the International Soil Reference and Information Centre (Batjes 1995) and the FAO-UNESCO Digital Soil Map of the World (FAO-UNESCO 1995). Physical soil parameters, such as hydraulic conductivity, bulk density, porosity, wilting point, and soil textures, were extracted from the Soils Program, interpolated from five arc-min (1/12°) to the 1/16° VIC grid, and then used to generate the values required to run the VIC model. Figure 2 shows examples of several soil parameter fields.

Table 1. VICGL land cover classes

Class	Label	Description
1	N-TeSp.1	Needleleaf Forest – temperate or sub-polar.1 – sub-alpine/sub-polar/open
2	N-TeSp.2	Needleleaf Forest – temperate or sub-polar.2 – high-elevation
3	N-TeSp.3	Needleleaf Forest – temperate or sub-polar.3 – mid-elevation
4	N-TeSp.4	Needleleaf Forest – temperate or sub-polar.4 – coastal/humid/dense
5	N-SpTa	Needleleaf Forest – sub-polar taiga
6	BE-TrSr	Broadleaf evergreen forest – tropical or sub-tropical
7	BD-TrSr	Broadleaf deciduous forest – tropical or sub-tropical
8	BD-TeSp	Broadleaf deciduous forest – temperate or sub-polar
9	MF	Mixed forest
10	S-TrSr	Shrubland – tropical or sub-tropical
11	S-TeSp	Shrubland – temperate or sub-polar
12	G-TrSr	Grassland – tropical or sub-tropical
13	G-TeSp	Grassland – temperate or sub-polar
14	SLM-SpP	Shrubland-lichen-moss – Sub-polar or polar
15	GLM-SpP	Grassland-lichen-moss – Sub-polar or polar
16	BaLM-SpP	Barren-lichen-moss – Sub-polar or polar
17	Wetland	Wetland
18	Crop	Cropland
19	Barren	Barren lands
20	Urban	Urban and built-up
21	Water	Water
22	Ice	Ice

2.2.3 Topography

Hydrologic processes are sensitive to spatial variation in topography, particularly as it affects temperature lapse rates, precipitation amount (e.g., orography) and phase, and solar loading. Topographic variability is considered by directly parameterizing the effect of elevation only; other topographic characteristics, such as slope and aspect, are currently ignored in this latest version of VIC. Sub-grid elevation variability in the VIC model is parameterized by sub-dividing each grid cell into elevation bands. These bands, in conjunction with user-specified precipitation and temperature gradients, are then used to determine the elevation-based sub-grid spatial variability in forcing temperature and precipitation. Elevation bands do not contain spatially explicit information in that discontinuous areas within certain topographic range are lumped into a single band. Elevation bands have been constructed using fixed 200--m elevation intervals, which is considered a reasonable compromise between vertical accuracy and increasing computational burden. Topographic parameterization is based on the Global Multi-resolution Terrain Elevation Data 2010 (GMTED2010) (Danielson and Gesch 2011). All topographic parameterization is based on processing of the 7.5 arc-second mean elevation product.

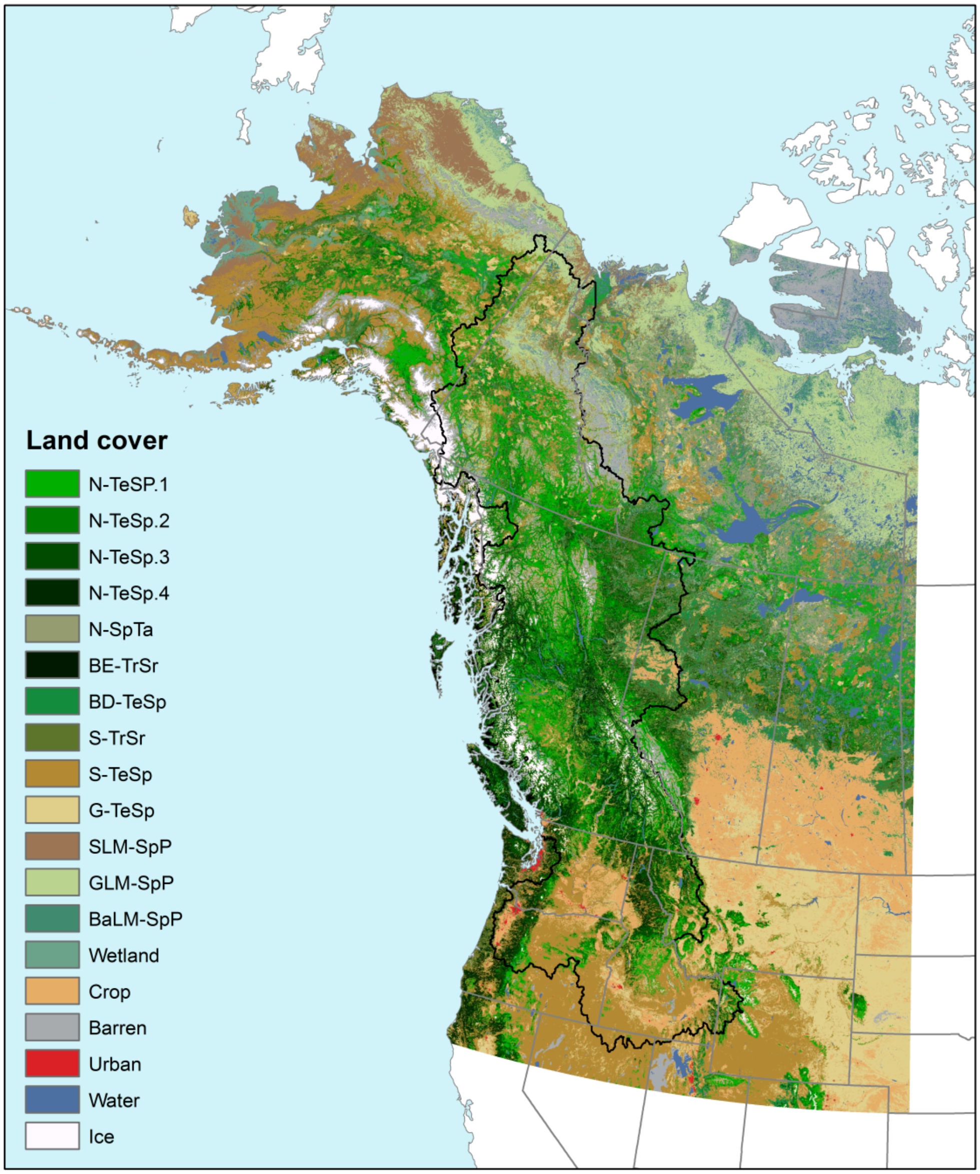

Figure 1. VIC land cover classification over the western North America (WNA) domain. Also shown is the outline for the PCIC modelling domain (black outline).

2.2.4 Hydrologic Response Units

Representation of sub-grid variability in the VIC model uses Hydrologic Response Units (HRUs), which are computational elements that are considered homogeneous from a hydro-climatological perspective. HRUs are created based on land cover classification and elevation; landscape elements are grouped into hydro-climatically homogeneous units if they have the same land cover class and are within the same elevation band. Sub-grid variability is determined by dividing each VIC grid cell into a collection of HRUs, where the HRU acts as the fundamental computational element of the model. The number of HRUs, and hence the effective model resolution, is then governed by the fidelity of the land cover classification (i.e., number of classes) and the vertical resolution employed (i.e. band discretization) (Figure 3). Note that HRUs do not retain any information on the original spatial organization of landscape elements as all areas of the same vegetation class within an elevation range are lumped together into a single HRU. Figure 4 shows the distribution of land cover by elevation band in the three main drainage basins.

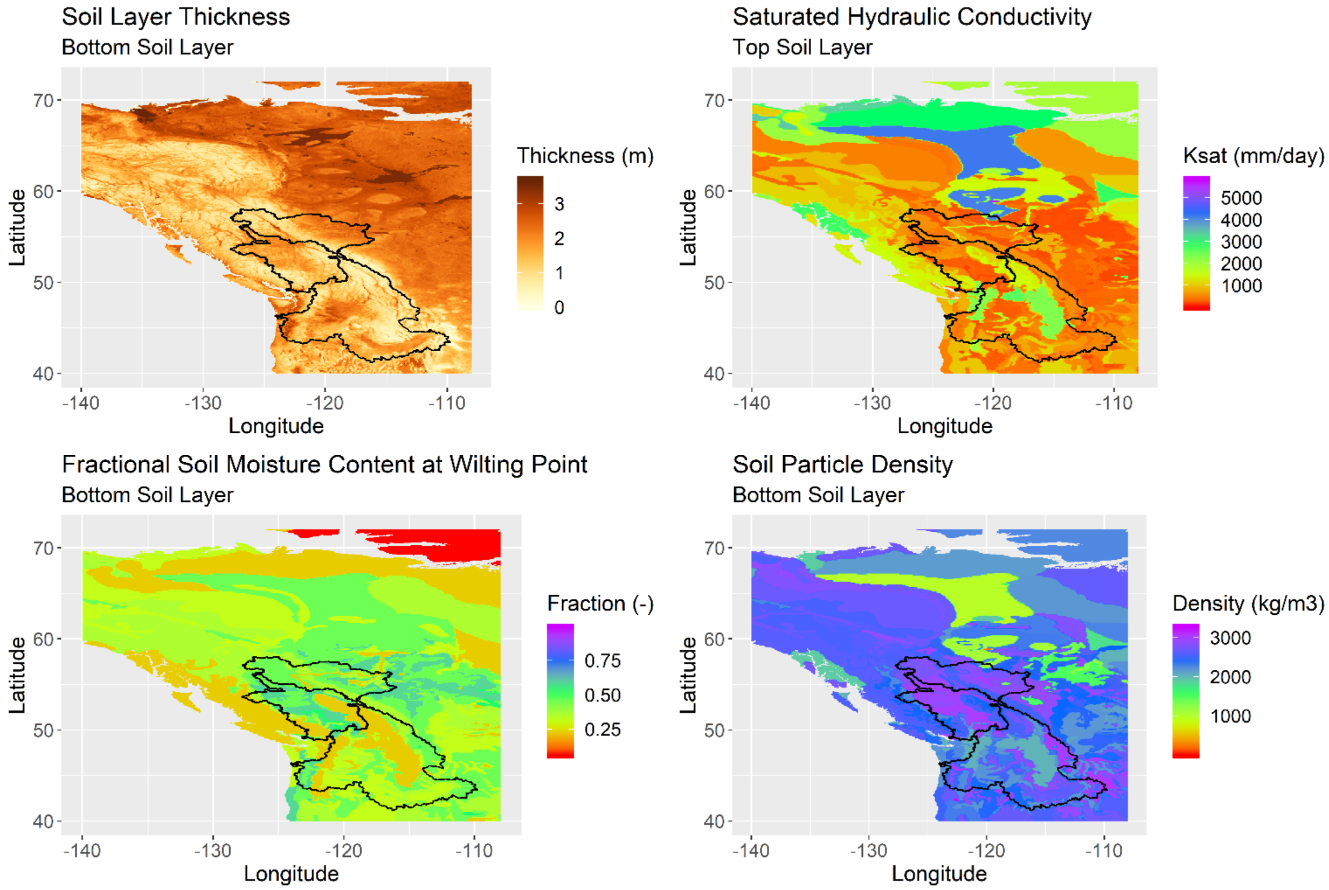

Figure 2. Example subset of soil parameters for the northwest North America Domain showing a) thickness of the bottom soil layer, b) saturated hydraulic conductivity of the topsoil layer, c) wilting point of the bottom soil layer, and d) particle soil density of the bottom soil layer.

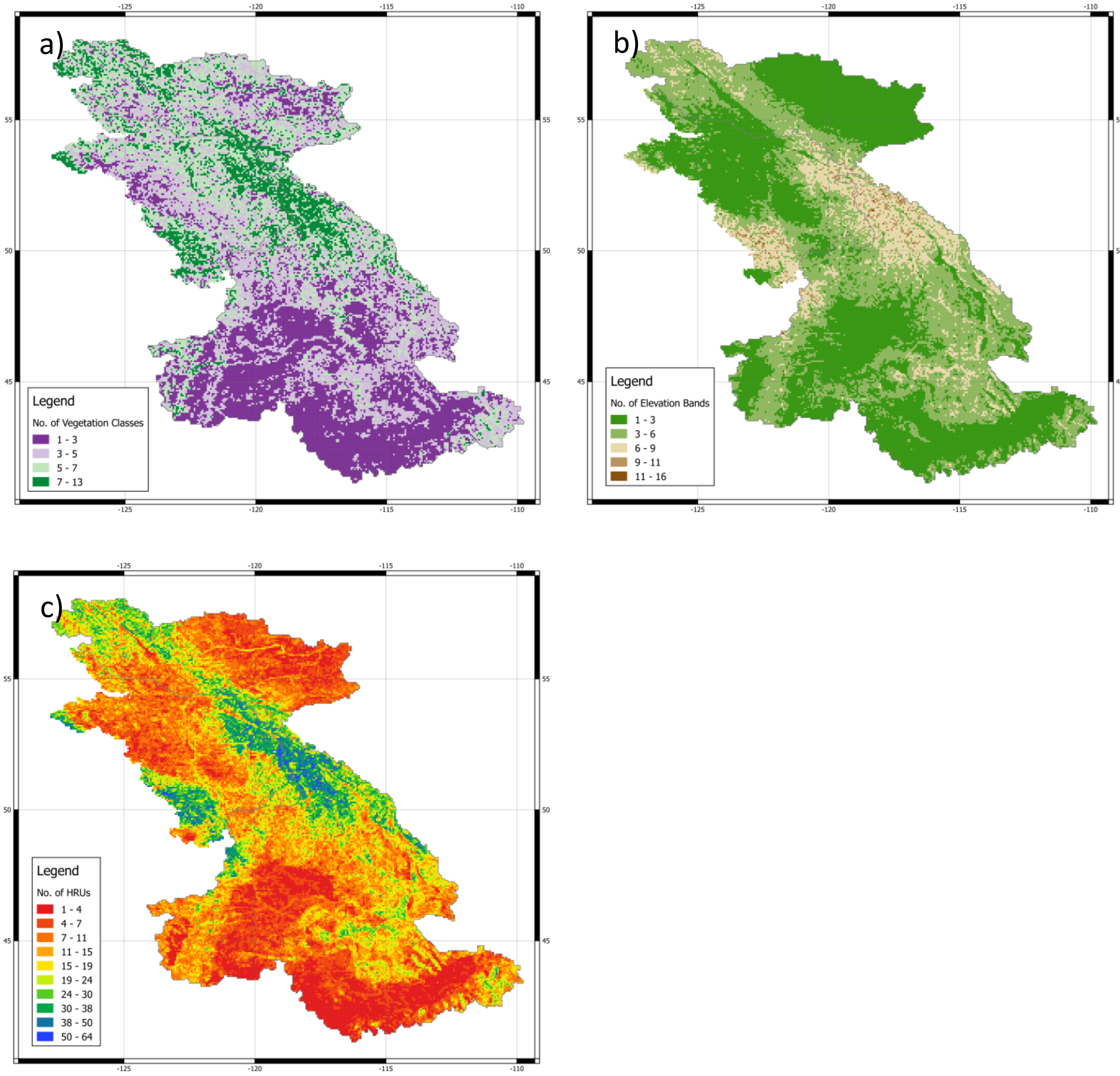

Figure 3. Spatial distribution of the number of a) vegetation classes, b) 200-m elevation bands, and c) hydrologic response units per VIC cell for the Peace, Fraser, and Columbia study areas.

a)

Columbia
Area = 696417 km^2
Minimum elevation = 0 m
Maximum elevation = 4268 m
Maximum number of bands per cell = 14
Number of land cover classes = 18
Number of cells = 20814
Number of HRUs = 267299

b)

Fraser
Area = 250238 km^2
Minimum elevation = 0 m
Maximum elevation = 3845 m
Maximum number of bands per cell = 16
Number of land cover classes = 16
Number of cells = 8452
Number of HRUs = 144643

c)

Peace
Area = 203969 km^2
Minimum elevation = 318 m
Maximum elevation = 3276 m
Maximum number of bands per cell = 11
Number of land cover classes = 17
Number of cells = 7485
Number of HRUs = 101348

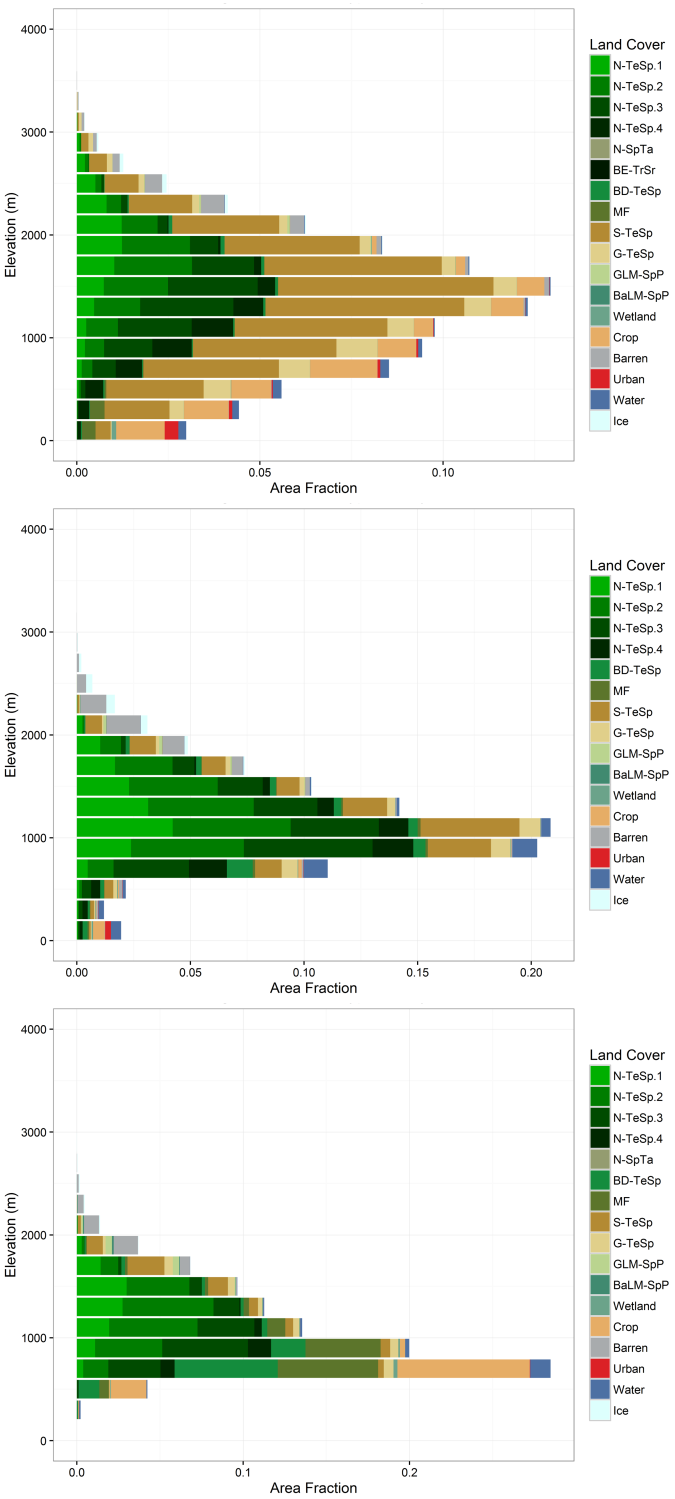

Figure 4. Distribution of vegetation by 200-m elevation bands with summary statistics for the a) Columbia at outlet, b) Fraser at outlet, and c) Peace (at Peace River, AB) drainages.

2.2.5 Routing network and drainage topology

The channel network is determined by tracing the ‘dominant’ flow direction through each grid cell (runoff from each cell can only flow in one direction). For efficiency, and to facilitate calibration (see Section 3), the study domain is sub-divided into small sub-basins and, hence, dependent by the location of suitable streamflow calibration sites. For the Peace and Fraser, sub-basins are mainly defined by the location of Water Survey of Canada gauges, although some locations coincide to BC Hydro and Rio Tinto Alcan project sites. In the Columbia, which is a highly regulated system, sub-basins delineation is governed by a mix stream gauge locations (operated WSC in Canada and USGS in the United States) and the locations of project sites operated by various public and private agencies (e.g., BC Hydro, FortisBC, US Corps of Engineers, US Bureau of Reclamation, US Bureau of Indian Affairs, Idaho Power Company). The resultant sub-basin and channel topology is shown in Figure 5, Figure 6 and Figure 7 for the Peace, Fraser and Columbia basins, respectively. The sub-basins are described in detail in Tables A1, A2, and A3 of Appendix A for the Peace, Fraser, and Columbia basins, respectively.

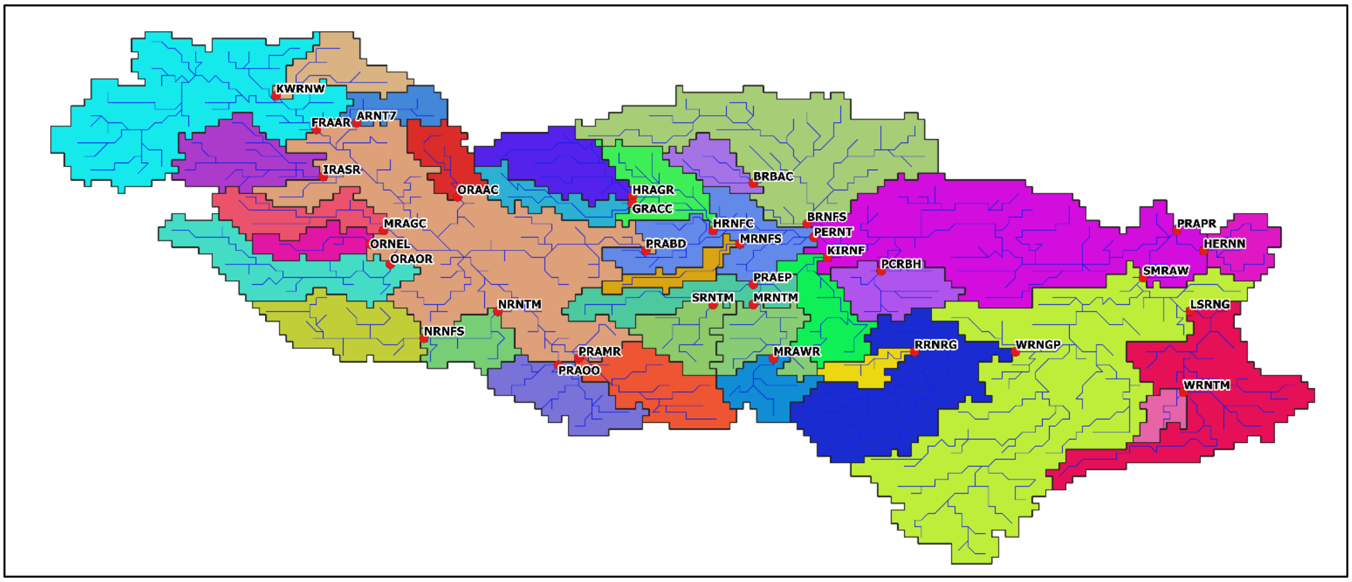

Figure 5. VIC-GL sub-basins (coloured polygons) and model drainage network (blue line) for the Columbia basin. Sub-basin outlets are show as red dots (with labels).

2.3 Forcing data

During model calibration, VIC-GL was forced using a gridded meteorological data set produced specifically for the 2nd generation modelling. This data set, called PNWNAmet, contains daily observations gridded at 1/16° (same spatial resolution as VIC-GL) with the variables of maximum and minimum temperature, precipitation and average wind speed (Werner et al. 2019). The PNWNAmet dataset was created over a domain covering northwest North America (40°N to 72°N and -169°W to -101°W). PNWNAmet was created using the trivariate thin plate spline interpolation method with the algorithm implemented by Nychka et al. (2017). Minimum temperature, maximum temperature and precipitation were interpolated separately using latitude, longitude and 1971-2000 climatology from ClimateWNA (v5.10) as predictors. Precipitation occurrence and square-root transformed precipitation amounts were interpolated separately on each day, combined, and transformed back to original units. After interpolation, the raw daily minimum/maximum temperature and precipitation surfaces were rescaled so that their climatological monthly means matched those of ClimateWNA following Hunter and Meetemeyer (2005). In addition, wind data is included from the 20th Century Reanalysis V2 (20CR2) (Compo et al., 2011). Werner et al. (2019) provide full details.

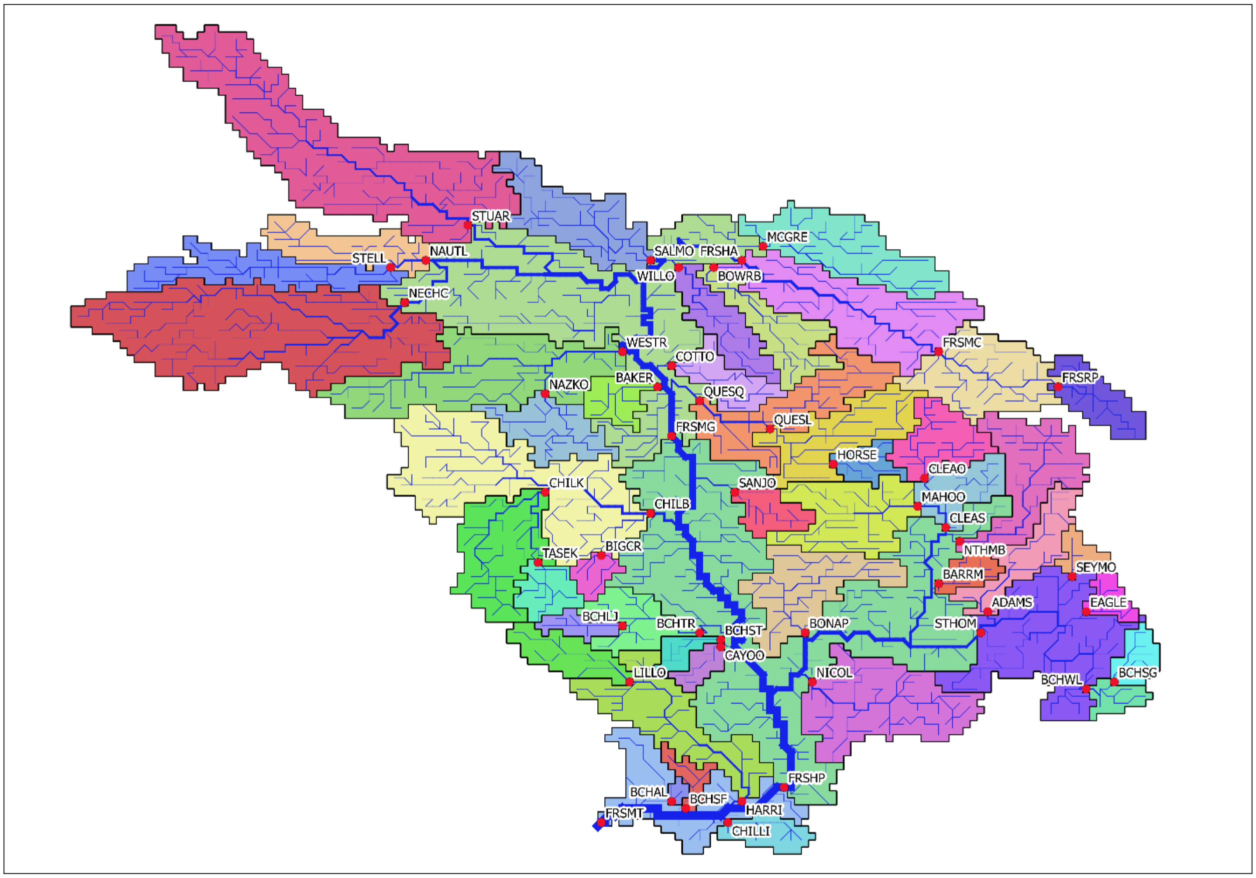

Figure 6. VIC-GL sub-basins (coloured polygons) and model drainage network (blue line) for the Fraser basin. Sub-basin outlets are show as red dots (with labels). The thickness of drainage network is proportional to upstream drainage area.

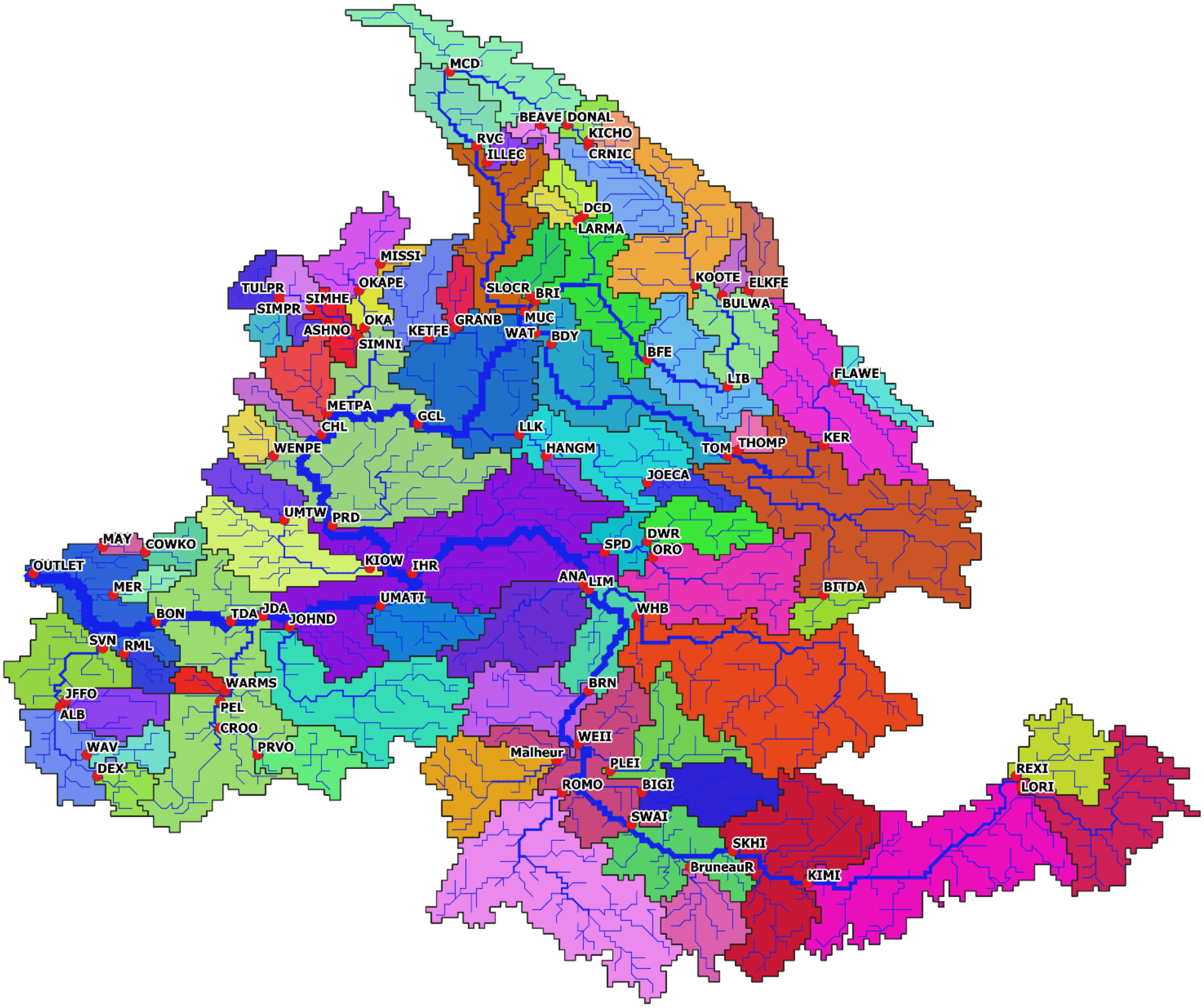

Figure 7. VIC-GL sub-basins (coloured polygons) and model drainage network (blue line) for the Columbia basin. Sub-basin outlets are show as red dots (with labels). The thickness of drainage network is proportional to upstream drainage area.

3 Model Calibration

3.1 Calibration Framework

Calibration of the VIC-GL model employs a multi-objective calibration paradigm. This approach exploits several different data sources to produce an optimized model based on explicitly constraining separate hydrologic processes. A multi-objective approach recognizes there are multiple ways in which a model can be best fit to the data. Hence, multi-objective problems tend not to have unique solutions. Using a Pareto-optimized set of parameters accepts that there is no “best” parameter set (model) and reflects uncertainty due to errors in the model structure, boundary conditions (i.e., meteorological data, hydrometric data, and soil, vegetation, and topography parameters) and observations. Realizations of the parameter vectors that constitute the Pareto set will also reflect the choice of objective functions.

Consider a hydrologic modelling application in which we are given *m* observations x_j, $j = 1, \ldots, m$ of a hydrologic variable (e.g., streamflow), *m* model output values y_j, $j = 1, \ldots, m$ of the same variable, and *n* model parameters p_k, $k = 1, \ldots, n$. The Euclidean geometrical spaces of the observations and model output is $\mathbb{R}^m$ and that of the parameters is $\mathbb{R}^n$. Due to the presence of constraints acting on the model parameters, their domain is restricted to $P \subseteq \mathbb{R}^n$, the feasible parameter domain. Let us consider a single objective function *h*, such that (Cavazzuti 2013)

$$\begin{aligned} &\mathbf{g}(\mathbf{p}) : P \subseteq \mathbb{R}^n \longrightarrow Y \subseteq \mathbb{R}^m, \;\; y_k = g_k(\mathbf{p}), \;\; k = 1, \ldots, m \\ &f(\mathbf{p}) : P \subseteq \mathbb{R}^n \longrightarrow H \subseteq \mathbb{R}, \quad h = f(\mathbf{p}, \mathbf{y}, \mathbf{x}) = f(\mathbf{p}, \mathbf{g}(\mathbf{p}) - \mathbf{x}) = f(\mathbf{p}) \end{aligned} \tag{1}$$

where *g* and *f* are the functions defining the output variables (i.e., the model) and the objective function respectively. Both the functions have the design space *P* for the domain, while their ranges are $Y \subseteq \mathbb{R}^m$ for the output variable, and the solution space $H \subseteq \mathbb{R}$ for the objective function. Hence, in a single objective context the purpose of model calibration is to manipulate the values of **p** to drive the difference between simulated and observed values, y_j and x_j, to be as close to zero as possible. More formally, the aim of optimization is

$$\min_{\mathbf{p}} f(\mathbf{p}), \qquad \mathbf{p} \in P \subseteq \mathbb{R}^n. \tag{2}$$

Practically this involves finding an optimal parameter vector **p*** such than $f(\mathbf{p}^*) < f(\mathbf{p})$ for all $\mathbf{p} \in P$.

The calibration of hydrologic models often lends itself well to a multi-objective approach. An optimization problem is considered multi-objective if it contains more than one objective function. For *z* objective functions a multi-objective optimization problem can be formulated as

$$\min_{\mathbf{p}} (f_1(\mathbf{p}), f_2(\mathbf{p}), \ldots, f_z(\mathbf{p})), \qquad \mathbf{p} \in P \subseteq \mathbb{R}^n \tag{3}$$

where P is again the feasible domain of parameter vectors. Due to conflicting objectives, multi-objective optimization does not typically produce a single solution **p*** that would be optimal for all objectives simultaneously. Therefore, attention is instead paid to the Pareto optimal solutions. Such solutions are those where none of the objectives can be improved without deteriorating at least one of the other objectives. Thus, a point in the feasible space **p*** is Pareto optimal if the vector of objective functions **f**(**p***) is non-dominated. The Pareto frontier is given by the set of the objective functions in the solution space whose vectors {**f(p)**} are non-dominated. The corresponding values of the model parameters {**p**} form the set of optimum solutions. The result of multi-objective calibration approximates the true Pareto frontier, which could be reached in the limit if an infinite number of sample sizes could be evaluated. The parameter values of this approximated frontier represent trade-off solutions providing the best compromises among the various objectives.

3.2 VIC-GL Calibration Overview

Calibration of the VIC-GL model can be considered within the context of the water balance, which is given as

$$P(t) = R(t) + E(t) + \frac{dS_{sn}(t)}{dt} + \frac{dS_{gl}(t)}{dt} + \frac{dS_{sl}(t)}{dt} + \frac{dS_{gd}(t)}{dt} + \frac{dS_{lk}(t)}{dt} \qquad (4)$$

where precipitation, P, into the basin at some time t is balanced by runoff, R, evapotranspiration, E, and changes in storage, S. Runoff includes all liquid water that exits a given domain as surface drainage and it usually considered the 'excess' component of the water budget. Evapotranspiration includes evaporation from the soil, evaporation of intercepted water from vegetation canopy, sublimation, and transpiration. The final component of the water balance includes hydrologic fluxes created because of changes in snow (*sn*), glacier (*gl*), soil (*sl*), groundwater (*gn*) and lake (*lk*) storage. To ensure a robust and physically plausible model, it is desirable to explicitly target as many of the components of (4) as is feasible (i.e., for which data exists). Such an approach is ideally suited to a multi-objective calibration approach, wherein separate objectives are used to constrain the different components of the water balance.

Precipitation, which drives the hydrology model, is constrained as a measured input. Nevertheless, P has potentially large biases, particularly at high elevations (Adam and Lettenmaier 2003; Adam et al. 2006). Runoff, a spatially distributed quantity, is not directly observed and streamflow is used as a proxy. With the advent of new satellite-based measurements of various hydrological phenomena, additional data is now also available to constrain additional components of the water balance, including evapotranspiration, snow, and glacier storage (see Section 3.3). Groundwater (here representing large regional aquifers and water stored in bedrock as opposed to local soil water) is not modelled in VIC-GL and its significance in BC is not well quantified (although it may be a significant source of error in other regions, such as the southern Columbia and Prairies) Lake storage is also not explicitly modelled in VIC-GL and its effect on model error has not been quantified.

The philosophy that governs the model calibration process is the desire to exploit the spatially distributed nature of the VIC-GL model. In an ideal setting, one would prefer to calibrate the model in a spatially explicit manner, i.e., grid cell by grid cell. However, as streamflow (or inflow) is typically the primary variable for water resources planning and management, the calibration design is dictated by the availability of discharge data. Hence, for calibration purposes the model domain is divided into sub-basins based on the location of hydrometric sites. This sub-division represents a trade-off between number of calibration sites and available record lengths; longer record lengths (but with fewer sites) include more hydro-climate variability to train the model robustly whereas more sites (with shorter records) allow for a more realistic spatial variability in the model parameters. We conduct calibration on each individual sub-basin, wherein model parameters are manipulated as spatially lumped quantities. The compromise is that spatial variability is maintained between sub-basins but is generally lost within sub-basins.

The results from preliminary calibration tests in several sub-basins were used to apply manual adjustments to parameters controlling transpiration and snow albedo decay (summarised in Table 2). Early runs indicated that simulated evapotranspiration, ET, was generally too low in several test basins (Similkameen, Tulameen and Ashnola). As transpiration forms the largest proportion of ET, adjustments were made to leaf area index and minimum stomatal resistance values in the vegetation library to increase transpiration. Monthly leaf area index for all classes was scaled by a factor of 1.25 and minimum stomatal resistance was reduced by a factor of 3 (which reflects minimum 'canopy' resistance as opposed to the original 'stomatal' resistance values) (Kelliher et al. 1995). Parameters controlling the rate of snow albedo decay were also adjusted to reduce the rate of snow albedo decay over time, generally resulting in increased snow accumulation and delayed onset of snowmelt. Based on these initial tests it was also determined that the temperature lapse rate, instead of using a spatially varying climatological value (derived from ClimateWNA), should be adjusted during calibration from a base value of 7.5°C/1000m. This adjustment generally results in steeper temperature lapse rates throughout the study domain and stronger gradients in snow accumulation with elevation. These adjustments were applied globally to the entire model domain.

Due to the conflation of the glacier runoff signal with other runoff sources in streamflow data, the parameters controlling glacier runoff, GLAC_KMIN, GLAC_DK and GLAC_A (Table *2*), were not calibrated for individual sub-basins. Instead, we used a single sub-basin, the Bridge River above La Joie Dam (BCHLJ; a heavily glaciated basin where discharge is considered very sensitive to glacier runoff) for calibration of these three parameters. Multi-objective calibration was carried out for BCHLJ and optimal values for the glacier runoff parameters were estimated using the average values from the best five runs. These optimal parameters values were than set globally for the entire study domain.

Modelled VIC-GL fluxes for all sub-basins were subsequently calibrated using the improved version of the non-dominated sorting genetic algorithm (NSGA-II) (Deb et al. 2002), an automatic evolutionary algorithm that solves the multiple objective global optimization problem. NSGA-II converges to and provides a sample of the Pareto frontier, which is a set of all parameter vectors that produce non-dominated values of the objective function vector. Implementation of the NSGA-II algorithm was accomplished using the *mco* R package (Mersmann 2014).

Table 2. VIC-GL Manual Calibration Parameters

Parameter	Adjustment	Value	Description
LAI	Scaling	1.25	Leaf area index
RMIN	Scaling	0.33	Minimum canopy resistance
SNOW_ALB_ACCUM_A	Absolute	0.95	Accumulation albedo decay parameter
SNOW_ALB_ACCUM_B	Absolute	0.40	Accumulation albedo decay parameter 2
SNOW_ALB_THAW_A	Absolute	0.85	Thaw albedo decay parameter
SNOW_ALB_THAW_B	Absolute	0.40	Thaw albedo decay parameter 2
TLAPSE	Absolute	7.50	Base temperature lapse rate (°C/km)
GLAC_KMIN	Absolute	0.05	Minimum glacier outflow factor
GLAC_DK	Absolute	0.50	Maximum increase in glacier outflow factor
GLAC_A	Absolute	15.00	Glacier outflow factor exponent

3.3 Automatic Calibration - Observed Data and Optimization Functions

3.3.1 Discharge

Calibration relied upon various sources of streamflow data (Table 3). For regulated systems calibration was performed against naturalized discharge provided by BC Hydro, Rio Tinto Alcan and the BC Ministry of Environment (effects of regulation removed) and by the Bonneville Power Administration (Columbia basin; effects of regulation and irrigation removed). The calibration period for discharge was 1991 to 2000, a period that represents a trade-off between a sufficiently long calibration period and large enough number of stations to discretize the study domain spatially. This period captures substantial low-frequency variability over the region, capturing several ENSO cycles (Climate Prediction Centre NOAA 2015).

Note that calibration to discharge assumes that the routing elements of the RVIC model are correct. The routing parameters of the RVIC model were determined a priori and set globally. The routing parameters used in the current application are based on a previous calibration using gauging locations in the Fraser River basin (see Schnorbus et al. 2010). Hence, discharge calibration effectively calibrates the VIC-GL simulation of Runoff and Baseflow, where Runoff is strictly surface runoff and Baseflow is sub-surface runoff from soil storage.

Table 3. Streamflow data sources

Data Source	Region	Conditions
Water Survey of Canada	Canada	Sites with unregulated discharge
United Sates Geological Survey	US	Sites with unregulated discharge
BC Hydro	BC	Naturalized discharge at BC Hydro generation sites in British Columbia (no regulation)
Rio Tinto Alcan	Nechako	Naturalized discharge for Nechako River sites regulated by the Nechako reservoir
BC Ministry of Environment	Fraser	Naturalized discharge for Fraser River sites regulated by the Nechako reservoir
Bonneville Power Administration	Columbia	Naturalized discharge in the Columbia basin (no regulation and no irrigation)

Different aspects of the streamflow regime are constrained by choosing a range of objective functions. For the current application of the VIC-GL model, three objective functions were used. The Kling-Gupta efficiency (KGE) goodness-of-fit measure was developed by Gupta et al. (2009) to provide diagnostic insight by decomposing model performance into correlation, bias and variability. The KGE is defined as

$$KGE = 1 - \sqrt{(r-1)^2 + (\alpha - 1)^2 + (\beta - 1)^2} \quad (5)$$

$$\alpha = \frac{\sigma_s}{\sigma_0}$$

$$\beta = \frac{\mu_s}{\mu_o}$$

where *r* is the linear correlation coefficient. Each of the terms in (5) have their optimum value at zero, such that the optimum KGE value is unity. From a hydrologic perspective usage of KGE makes sense, because in general we are interested in reproducing temporal dynamics (measured by *r*), as well as preserving the distribution of flows (flow duration curve), which can be summarized by the first and second moments (measured by α and β). Values for KGE range from one (perfect fit) to $-\infty$. Good model performance is deemed to occur when KGE exceeds zero, which can occur for various combinations of *r*, α and β, as shown in Figure 8. Positive KGE values occur when *r*, α and β are bounded approximately by $0 \leq r \leq 1$, $0 < \alpha < 2$, and $0 < \beta < 2$.

The Heteroscedastic Maximum Likelihood estimator (HMLE) (Sorooshian and Dracup 1980; Sorooshian et al. 1983) is the maximum likelihood, minimum variance, asymptotically unbiased estimator when the errors in the output data are Gaussian, zero mean, and uncorrelated and have nonstationary variance in time. Use of the HMLE assumes that the variance of the errors relates to the level of the output (magnitude of the flows), believed to be a common occurrence in streamflow data. The HMLE is defined as

$$HMLE = \left\{\sum_{t=1}^{n} w_t \varepsilon_t^2\right\}\left\{n\left[\prod_{t=1}^{n} w_t\right]^{1/n}\right\}^{-1} \tag{6}$$

where $\varepsilon(t)$ is $y_s(t) - y_o(t)$, $w(t)$ is $f(t)^{2(\lambda-1)}$ and λ is the Box-Cox transformation parameter (Box and Cox 1964). The parameter λ is estimated by setting $f(t) = y_o(t)$ and optimizing for each new parameter vector using the `optimize` package in R (R Core Team 2016). The HMLE places greater weight on lower values, which are considered to have smaller errors and more information, than higher values.

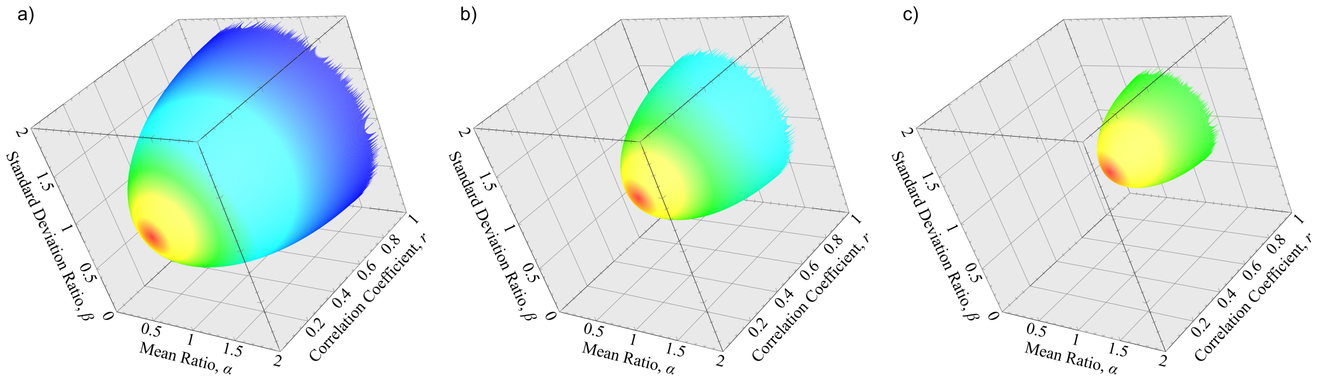

Figure 8. Surface delineating permissible values of r, α and β when the KGE threshold is a) zero, b) 0.5, and c) 0.75. The color of the surface denotes the local radius in the α-β plane.

A third objective function is the Nash-Sutcliffe Efficiency (NSE) (Nash and Sutcliffe 1970), defined as

$$NSE = 1 - \frac{\sum_{t=1}^{n}\{y_s(t) - y_o(t)\}^2}{\sum_{t=1}^{n}\{y_o(t) - \mu_o\}^2} \tag{7}$$

The NSE is essentially the mean squared error normalized by the standard deviation of observed values. NSE is as a classic skill score, where skill is the comparative ability of a model with respect to a baseline model, which in this case is the mean of the observations. In this context if NSE ≤ 0 the model is no better than using the observed mean as a predictor. An NSE equal one indicates perfect model performance. In our calibration procedure, the NSE is applied using log-transformed discharge, which we call the LNSE objective (NSE of log-transformed discharge). The LNSE objective tends to place more uniform emphasis throughout the entire flow range and therefore tends to encourage parameter sets that have improved performance during recession and low flow periods.

Observed discharge at any location represents the total discharge generated by the entire upstream areas. For 2nd-order of higher sub-basins, VIC-GL runoff and baseflow integrate to produce local discharge only. Consequently, simulated local discharge is combined with observed discharge flowing into the sub-basin from upstream sites prior to calibration. Unfortunately, the structure of the RVIC model does not allow the specification of in-channel flow as an upstream boundary condition. Therefore, discharge ($m^3\ s^{-1}$) from all upstream sites was converted to surface runoff ($mm\ d^{-1}$) and added to the appropriate cell in the flux file. However, as RVIC routes all runoff through the VIC cell prior to adding it to the channel network, the added runoff had to be reverse convolved of in-grid routing prior to adding it to the appropriate upstream VIC cell using the following procedure

$$r_c(t) = \left\{\left[q_c(t) - \sum_{j=2}^{n} r_c(t-j+1)\cdot u(j)\right] u(1)^{-1}\right\} 86400 * 1000/A_c \tag{8}$$

where *u* is the grid-cell unit hydrograph, *q* is discharge observed at upstream cell *c* and *A* is the area (m^2) of grid cell *c*. Reverse convolution is conducted at a daily time step using the daily unit hydrograph described in Table *4*.

Table 4. Daily unit hydrograph used for reverse convolution

Day, *j*	u(*j*)
1	0.631978
2	0.328619
3	0.036218
4	0.003185

3.3.2 Evapotranspiration

Observed evapotranspiration data is provided by the LandFlux-EVAL multi-data set synthesis (Mueller et al. 2013). This data set is a monthly global synthesis of land evapotranspiration estimates from 14 global data sets for the period 1989 to 2005. The data sets can be categorized into three groups: diagnostic data derived from in situ or satellite-based observations, estimates calculated via land surface models driven with observation-based forcing, or estimates obtained as output from atmospheric reanalyses. The various products are merged and provided as set of gridded statistics (minimum, maximum, median, mean, 25th percentile, 75th percentile and standard deviation). The original merged product, which has a spatial resolution of 1°, was re-gridded to the spatial resolution of VIC-GL (1/16°) using distance-weighted average remapping using the `remapdis` function in cdo, (CDO 2015). The re-gridded product is then used to calculate basin-wide monthly values of the minimum, maximum and median ET (e_{min}, e_{max} and e_{med}, respectively).

We use a membership function to quantify how well simulated ET values, e_s, fall within the maximum-minimum range of the 'observed' basin-wide monthly ET data. Specifically, we employ an objective based on the bell-shaped membership function (Zhao and Bose 2002)

$$BMF_{ET} = \frac{1}{n}\sum_{t=1}^{n}\left\{\frac{1}{1+\left|\frac{e_s(t)-c(t)}{a(t)}\right|^{2b}}\right\} \tag{9}$$

where the width parameter, a, is set equal to $[e_{max}(t) - e_{min}(t)]/6$, the shape parameter, b, is set equal to a constant value of 2, and the parameter c, the centre of the curve, is set equal to $e_{med}(t)$. The bell function is smooth and non-zero at all points, with a maximum of one at e_{med}. Although the bell function does not equal zero for values below (above) the e_{min} (e_{max}), the function rapidly approaches zero beyond these limits. The BMF as defined is essentially the mean of the individual monthly membership calculations, with values ranging from one (best) to zero (worst). The calibration period for monthly ET is identical to that of streamflow, which is 1991 to 2000 (n = 120).

3.3.3 Snow Covered Area

Snow covered area (SCA) data is used to constrain the snow accumulation and melt process in VIG-GL. Observed snow covered area (SCA) is provided by the MODIS/Terra Snow Cover Monthly L3 Global 0.05Deg CMG, Version 6 (MOD10CM) (Hall and Riggs 2015). The MOD10CM product is a satellite-based global estimate of SCA based on the Normalized Difference Snow Index (NDSI). SCA is the snow cover fraction for each 0.05° grid. A time series of basin wide monthly SCA for each sub-basin was produced by taking the weighted average of the overlapping 0.05° grids for each month. Area averages were calculated using the `extract` function from the *raster* R package (Hijmans 2016), using normalized weights based on the fraction of each cell within the sub-basin. The calibration period for SCA is January 2001 to December 2005 (n = 60). We use the KGE as the objective function for assessing SCA.

3.3.4 Glacier Mass Balance

For glaciated basins, glacier mass balance data provides an additional calibration constraint. Observations were the geodetic thinning rates, ΔH, estimated for the period 1985 to 1999 by Schiefer et al. (2007). Thinning rates were provided as a basin-wide annual average, obtained by averaging a 100-m resolution difference grid over the glaciated regions of each sub-basin (as defined by the 1/16° sub-basin boundaries) and averaging over the measurement period (n=15 years). Uncertainty in the thinning rate was estimated as ±3.0 m for the observation period, based on a BC-wide standard error estimate of ±0.19 m/a reported by Schiefer et al. (2007). Thickness changes were converted to water equivalent using an area-weighted density for firn (550 kg m^{-3}) in the accumulation zone and ice (910 kg m^{-3}) in the ablation zone. Area weighting used accumulation area ratios of 0.15 to 0.6 (conversion factors of 0.85 to 0.7) (B. Menounos, personal communication). The lower and upper estimate of measured geodetic mass balance in water equivalent were then estimated as

$$
\begin{aligned}
b_l &= min\,\{0.7(\Delta H - 3), 0.85(\Delta H - 3)\} \\
b_u &= max\{0.7(\Delta H + 3), 0.85(\Delta H + 3)\}
\end{aligned}
\tag{10}
$$

with a 'mid-point' estimate calculated as

$$b_m = (b_u - b_l)/2. \tag{11}$$

We use the following bell membership function to assess model performance

$$BMF_B = \frac{1}{1 + \left|\frac{b_s - b_m}{(b_u - b_l)}\right|^2}. \tag{12}$$

3.3.5 Multi-objective Optimization Function

The generic multi-objective problem specified by (3) now becomes

$$\min_{\mathbf{p}}\big(f_1(\mathbf{p}), f_2(\mathbf{p}), f_3(\mathbf{p}), f_4(\mathbf{p}), f_5(\mathbf{p}), f_6(\mathbf{p})\big), \qquad \mathbf{p} \in P \subseteq \mathbb{R}^n \tag{13}$$

where f_1 = -KGE$_Q$, f_2 = HMLE$_Q$, f_3 = -LNSE$_Q$, f_4 = -BMF$_{ET}$, f_5 = -KGE$_{SCA}$, and f_6 = 1_G(-BMF$_B$), where 1_G is equal 1 if glacier area > 0 km^2 and equal 0 otherwise. Note the use of negative signs for KGE, BMF, and LNSE to accommodate function minimization. Subscripts Q, ET, SCA and B refer to discharge, evapotranspiration, snow cover area, and glacier mass balance, respectively. The feasible parameter domain for individual element of the vector **p** are set by specifying parameter ranges (see Section 3.4).

3.4 VIC-GL Model Parameters

Most VIC-GL parameters are treated as 'observed' and not modified during the calibration process. Only a small set of model parameters are used to calibrate the model, chosen either because they are the most sensitive parameters (Demaria et al. 2007) or the they tend to reflect the more empirical aspects of the model (and as such may not have a physically measurable meaning). The VIC-GL parameters selected for adjustment during automatic calibration are described in Table *5*. For each iteration of the calibration process, a parameter vector $\Theta = \{\theta_1, \theta_2, \dots, \theta_k\}$ was sampled by adjusting the individual elements of a base parameter vector $\Phi = \{\phi_1, \phi_2, \dots, \phi_k\}$ using three possible procedures (depending upon the parameter):

- Absolute – original value replaced with $\theta_i = p_i$
- Scaling – original value multiplicatively scaled as $\theta_i = p_i\phi_i$
- Delta – original value additively scaled as $\theta_i = p_i + \phi_i$

where $\{p_1, p_2, \ldots, p_k\}$ is a random vector sampled from the ranges given in Table *5*. Parameter adjustments, p, were constrained to a precision of 0.001, except *BI* and *DS* that used a precision of 0.0001.

Table 5. VIC-GL Automated Calibration Parameters

Parameter	Adjustment	Range[‡]	Description (with units where applicable)
BI	Absolute	0.5000 - 0.0001	Infiltration partitioning parameter
DS	Absolute	0.2000 - 0.0001	Baseflow curve parameter
DSMAX	Scaling	2.000 - 0.001	Maximum baseflow
WS	Absolute	0.950 - 0.200	Baseflow curve parameter
EXPN	Scaling	3.000 - 1.000	Vertical change in hydraulic conductivity in all soil layers
D3	Scaling	3.000 - 0.500	Depth of third soil layer
NEWALB	Absolute	0.950 - 0.850	Albedo of new snow
PADJ_R	Absolute	2.000 - 0.250	Precipitation adjustment for rainfall
PADJ_S	Absolute	2.000 - 0.250	Precipitation adjustment for snowfall
TLAPSE	Delta	2.500 - -2.500	Temperature lapse rate (°C/km)
GLACALB	Absolute	0.600 - 0.200	Glacier albedo (when $1_G = 1$)
GLACRF	Absolute	1.000 - 0.000	Snow redistribution to glaciers (when $1_G = 1$)

[‡] Precision reflected by number of decimal places in the range values

The *BI* parameter controls the partitioning of net precipitation or snowmelt into surface (or quick) runoff and infiltration (which ultimately becomes evaporation, transpiration or baseflow). The *DS* and *WS* parameters control the shape of the baseflow curve (specifically the location of the inflection point from where baseflow transitions from a linear to a non-linear function of soil moisture). *DSMAX* specifies the maximum baseflow velocity and base values are set as a function of local slope. This parameter is adjusted using the scaling approach to maintain the original spatial variability. The *EXPN* parameter (one per soil layer) describes the exponential change of hydraulic conductivity with depth. A nominal base value is estimated as $3+2/L$, where L is the pore size index (which is a function of soil texture). The EXPN parameter is adjusted by using the same scaling factor for each soil layer. *D3* is the depth of the third soil layer, with nominal base values estimated as a function of local elevation and slope. Values for *D3* are scaled during calibration to maintain the original underlying spatial variability. *NEWALB* is the albedo of new fallen snow. *PADJ_R* and *PADJ_S* are precipitation adjustment factors for rainfall and snowfall, respectively. *TLAPSE* is the temperature lapse rate in each grid cell. Although a base value was originally estimated per cell, using local temperature gradients estimated from Climate WNA, preliminary testing indicated that a global base value of 7.5°C/1000m was more effective. *GLACALB* is the albedo of glacier ice. *GLACRF* is a parameter that controls the redistribution of snowfall between non-glacier and glacier HRUs per elevation band.

It is recognized that the use of separate precipitation adjustment parameter for rain and snow may introduce artefacts in the climate change projections. For forcing the hydrologic simulations, only precipitation is downscaled from the driving global climate experiment, and the partitioning into rain and snow is estimated in VIC-GL (using air temperature thresholds). Hence, under future climates the precipitation trend supplied by a GCM will be partitioned into separate rain and snow trends by VIC-GL, depending on the temperature trend (i.e., rainfall may increase and snowfall may decrease). Consequently, applying independent precipitation adjustments to rain and snow may inadvertently produce a precipitation trend in VIC-GL that differs from that in the driving climate experiment. Therefore, in practice the PADJ_R and PADJ_S parameters are always set equal during model calibration.

3.5 Parameter Selection

Once the final set {**p**} of optimum solutions has been generated, typically only one solution from this set is selected for model projections. The process of parameter selection is conducted in two stages. The first stage is to adopt a fuzzy approach to ranking the parameter vectors in the Pareto optimum solution. For a given parameter vector, **p**, a fuzzy score is calculated as the weighted-average of individual membership values for each normalized objective function value as

$$S = \sum_{r=1}^{z} w_r \, \mu_r(\tilde{f}_r(\mathbf{p})) \qquad \mathbf{p} \in P \subseteq \mathbb{R}^n \tag{14}$$

where $\tilde{f}_r(\mathbf{p})$ is $f_r(\mathbf{p})$ normalized to the range (0,1), $\mu_r(\cdot)$ is the sigmoidal membership function

$$\mu_r(x; a, b) = \frac{1}{1 + e^{-a_r(x - b_r)}}, \tag{15}$$

where *a* determines the steepness of the function (if *a* is negative the function is open to the left) and *b* locates the value of *x* where μ_r = 0.5, and *w* is the weight given to each objective function, where $\sum_r w_r = 1.0$. The parameter values for equations (14) and (15) are given in Table 6.

Table 6. Parameter values for Fuzzy Score calculation

Objective	Parameter value with (without) glaciers		
	a	*b*	*w*
$-\text{KGE}_{\text{Q}}$	-20	0.25	0.3 (0.4)
HMLE_{Q}	-10	0.5	0.1 (0.1)
$-\text{LNSE}_{\text{Q}}$	-10	0.5	0.3 (0.3)
$-\text{BMF}_{\text{ET}}$	-10	0.5	0.05 (0.1)
$-\text{KGE}_{\text{SCA}}$	-10	0.5	0.05 (0.1)
$-\text{BMF}_{\text{B}}$	-20	0.25	0.2 (0.0)

For the second stage of parameter selection, the final performance scores are ranked, and the top ten vectors are selected for further evaluation. The second evaluation stage involves a heuristic assessment of model performance, based on a visual assessment of several different chart types, plus a deeper inspection of additional metrics not used in the automated calibration process. The final parameter set is the one subjectively chosen as the ‘best’.

4 Verification Results

Although the model has been calibrated, validation of model performance with independent data is necessary to ensure the model parameterization is robust, which is important to establish confidence in the model's ability to extrapolate to climatic conditions unobserved during the historical period.

The presentation and discussion of model validation is organized into two main sections. Model validation is described by first reviewing the split-sample performance metrics for all sub-basins in Section 4.1. This will be followed by a validation of VIC-GL's performance in simulating metrics which were not included in model calibration, with a focus on the Fraser basin (Section 4.2). A more detailed look at snow cover area fraction and evapotranspiration for the entire Fraser basin are the subjects of Sections 4.2.2 and 4.2.3, respectively. The simulation of basin-scale glacier area and mass balance, which incorporates the use of glacier dynamics modelling, is reviewed in Sections 4.2.4.

4.1 Split-Sample Validation

We used a split-sample approach to model validation (Klemeš 1986), where the available observed data is split into two periods, one of which is used for calibration and the other for validation. However, although Klemeš (1986) recommends using each of the periods for calibration and validation in turn, computational limitations precluded us from doing this.

As per model calibration, and validation is based on the comparison of simulated to observed discharge (Q), evapotranspiration (ET), snow cover area (SCA) and, where applicable, basin-average glacier surface mass balance (B). Validation performance is evaluated using the metrics and evaluation periods described in Table 7. Performance metrics for discharge include the Kling-Gupta efficiency (KGE; Gupta et al. 2009), the Nash-Sutcliffe efficiency for log-transformed discharge (LNSE; Nash and Sutcliffe 1970), the heteroscedastic maximum likelihood Estimator (HMLE; Sorooshian and Dracup 1980) and the bell membership function (BMF; Zhao and Bose 2002). Model performance metrics are described in detail in Section 3.

Table 7. Calibration and validation metrics and evaluation periods

	Discharge	Evapotranspiration	Snow Cover	Glacier Mass Balance
Statistics	KGE, LNSE, HMLE	BMF	KGE	BMF
Calibration Period	1991-2000	1991-2000	2000-2005	1985-1999
Validation Period	2001-2007	2001-2005	2006-2010	1985-1999$^{\$}$

Two differences in model application for simulation of discharge and glaciers between calibration and validation runs are discussed. For non-headwater basins, the model was calibrated to local flow only, where simulated discharge was a combination of local discharge and observed inflow from upstream basins. During the validation process, however, discharge at the basin outlet is simulated from the total upstream area. The numerical schemes used to model glacier dynamics have known limitations whereby mass can be created in regions of extreme topography (Clarke et al. 2015b). Although the numerical scheme used in the RGM has been adapted to mitigate this issue (Jarosch et al. 2013), we note that the problem still persists in certain locations when observed surface topography and modelled bed topography are inconsistent (i.e. the digital elevation data used to estimate bed topography differs from that used to parametrize VIC-GL). Consequently, for simulations using glacier dynamics, an initial surface topography is estimated using a lengthy spin-up procedure (see Section 5.2). Therefore, during the calibration process glacier area was kept static (based on circa. 2005 land cover) and the calibration runs were relatively short (1985 to 2005 with a 2-year spin-up period). The simulations used for model validation, however, included coupled glacier dynamics to simulate changes in glacier area and these simulations were run for a much longer integration period (1945 to 2012). Calibration used observed glacier cover, whereas validation runs required an initialization of a 1945 glacier state. Hence, the validation performance measures for the discharge and glacier mass balance incorporate additional model complexity and feedbacks that were not constrained during the calibration process. Validation metrics for all sub-basins are summarized in Appendix A .

4.1.1 Discharge

As expected, there is some loss of model accuracy during the validation period, as seen in the changes in KGE_Q, LNSE_Q and HMLE_Q (Figure 9). This is likely due to some model overfitting, however, for higher-order basins the validation statistics also represent errors in discharge simulated in upstream basins. In addition, for glaciated basins the incorporation of glacier dynamics adds feedbacks between glacier area changes and glacier melt and runoff not explicitly accounted for during model calibration.

4.1.2 Evapotranspiration

The median BMF_ET value is quite stable between calibration and validation and model performance is quite reasonable (Figure 9). Note that the basis of the BMF_ET values is based on comparison with the ensemble median of the observations, and in most of the cases the simulated ET values fall within the minimum to maximum range of the observation ensemble (not shown). During both calibration and validation simulated ET is, when compared to the observation ensemble median, negatively biased in the Columbia and Fraser, but positively biased in the more northerly Peace (Figure 11).

4.1.3 Snow Cover Area Fraction

Simulation of SCA is also very stable, and KGE_SCA and relative bias values change very little between calibration and validation (Figure 9 and Figure 11). SCA is simulated quite well in the Peace and Fraser, with validation KGE values all greater than 0.70 (Figure 9; Appendix A, Tables A5 and A6). Results are not as strong for the Columbia, where results vary widely (Figure 9; Appendix A, Table A7). There is also a bias in the SCA values, with the more northerly Peace and Fraser sub-basins showing a positive bias and the Columbia sub-basins showing a negative bias (Figure 11). Larger snow cover area (and presumably longer snow cover duration) than observed may be acting to suppress ET, which could partially account for the lower simulated ET values.) Overfitting, however, is not a large issue, as the KGE_SCA statistics do not vary considerably between calibration and validation (Figure 9). KGE_SCA and SCA bias are summarized by basin in Appendix A, Tables A5, A6 and A7 for the Peace, Fraser, and Columbia, respectively.

VIC-GL models snow cover as a binary process, where if a hydrologic response unit (HRU) in each cell contains SWE > 0, then the entire HRU area is considered snow covered. Hence, overestimation of snow cover is not unexpected. It is also plausible that the remote sensing-based observations also underestimates snow cover area. The algorithm for MOD10CM product filters out cells with monthly SCA < 10%, (SCA is set to 0% in these cases) as these are assumed to be erroneous snow detections. It is also not clear how well the latest MODIS algorithms detects snow cover in forested terrain.

4.1.4 Glacier Surface Mass Balance

The incorporation of dynamic glaciers in the validation run as compared to static glaciers in the calibration results in an apparent degradation of model accuracy (Figure 9). The difference between calibration and validation results is due exclusively to the addition of glacier dynamics in the validation integration (statistics for both use the same observed thinning rates). Inclusion of glacier dynamics in the validation runs adds additional complexity and feedbacks that were not accounted for during model calibration. For instance, although the VIC-GL model is well calibrated to sub-basin-average mass balance rates, there are likely errors in the spatial variability of the estimated mass balance field used to force the dynamics model. The dynamics model itself is also very sensitive to errors in bed topography. Both errors in mass balance and bed topography can result in diverging trajectories between actual and simulated glacier area and relief over time. Errors in glacier dynamics can also result in altitudinal feedback, whereby errors in simulated surface elevation and glacier hypsometry lead to errors in the estimation of surface mass balance rates (via the effect of elevation on temperature and precipitation phase and amount). The value of BMF_B for each sub-basin is shown Appendix A, Tables A5, A6 and A7 for the Peace, Fraser, and Columbia, respectively.

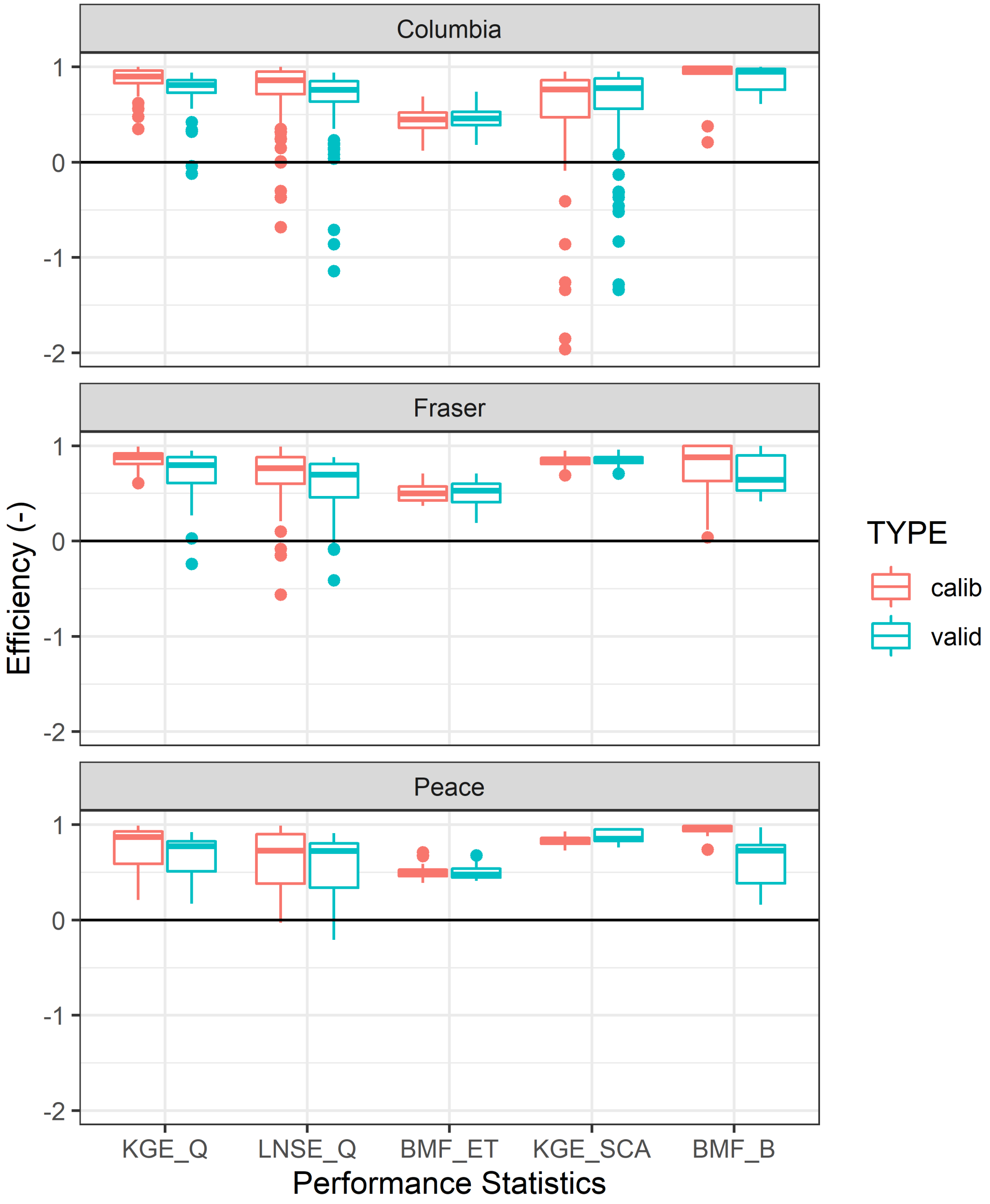

Figure 9. Calibration and validation results for streamflow KGE (KGE_Q), streamflow log Nash-Sutcliffe (LNSE_Q), membership function for evapotranspiration (BMF_ET), snow cover KGE (KGE_SCA), and glacier mass balance membership function (BMF_B). Results are summarized as box plots by major study basin, where the thick line shows the median, the box shows the interquartile range (range between the 1st and 3rd quartiles, or 25th and 75th percentiles), whiskers extend to 1.5 times the interquartile range, and outliers are shown as dots.

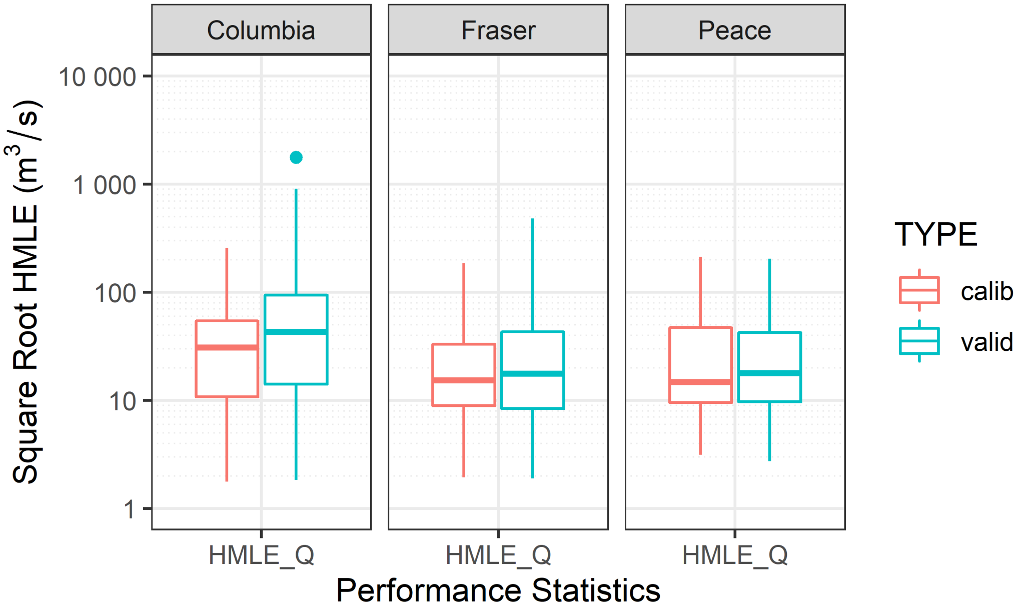

Figure 10. As per Figure 9, but for the Heteroscedastic Maximum Likelihood metric for streamflow (HMLE_Q).

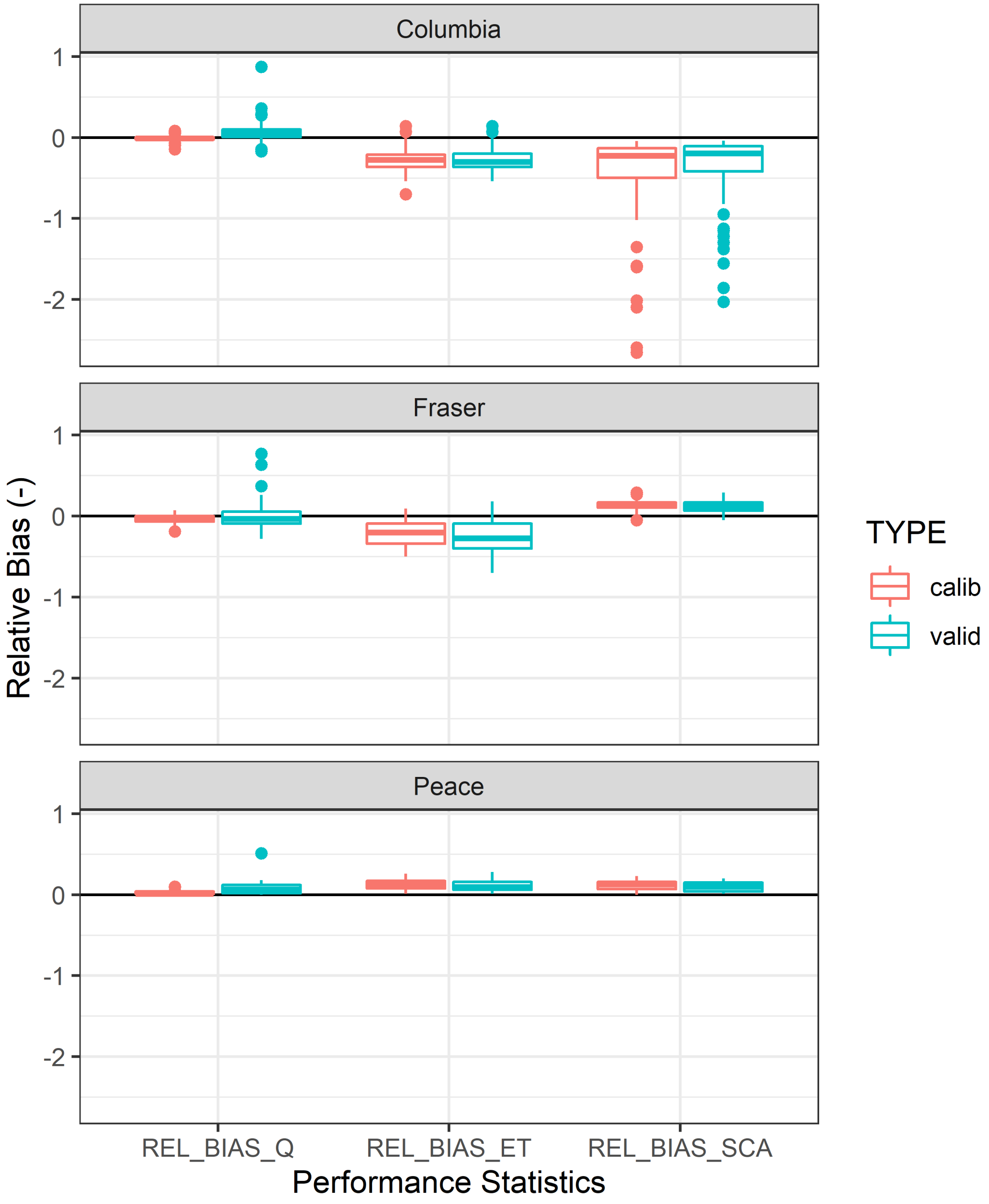

Figure 11. As per Figure 9, but for the relative bias in daily streamflow (REL_BIAS_Q), monthly evapotranspiration (REL_BIAS_ET) and monthly snow cover (REL_BIAS_SCA).

4.2 Out-of-Sample Validation

Out-of-sample validation compares model results with observational data not used in original calibration (such as SWE, and glacier area), or considers data used in original validation, but at a different spatial scale (e.g., snow cover area and evapotranspiration). As such, this type of validation is a very stringent test of model robustness. Results are currently based only the Fraser River basin.

4.2.1 Snow Water Equivalent

In this section we focus on model's skill in simulating snow accumulation. As snow accumulation observations were not used as part of model calibration, this is an independent assessment of model skill. Model performance was assessed via comparison to manual snow survey (MSS) data collected and published by the BC Ministry of Environment and Climate Change Strategy - Knowledge Management (https://www2.gov.bc.ca/gov/content/environment/air-land-water/water/water-science-data/water-data-tools/snow-survey-data). Seasonal peak snow accumulation averaged over 1971 to 2000 is assessed by comparing snow water equivalent (SWE) measured on or about April 1st with that simulated by VIC-GL in grid cells in which the MSS stations are located. To make comparison as representative as possible, we used band values for SWE from the cell band with median elevation closest to that of the station elevation. The stations used were filtered such that site elevation, z, exceeds 500 m, ten or more years of observations are available during 1971-2000, and the absolute difference between site elevation and grid cell average elevation, $|dz|$, is less than 1000 m. Seventy-five MSS stations located throughout the Fraser basin were used, with the station meta-data provided in Appendix A, Table A4.

Table 8. Model performance statistics for Basin-integrated variables

Statistic[§]	Peak SWE	Monthly SCA	Monthly ET	GLAC_AREA	GLAC_MBAL
mean_{obs}	504.2 mm	0.47	1.1 mm	3443.5 km^2	-7.4 m
mean_{sim}	374.0 mm	0.54	0.9 mm	3495.4 km^2	-3.6 m
Bias	-130.1 mm	0.08	-0.2 mm	52.9 km^2	3.8 m
RBias	-0.26	0.16	-0.18	0.015	-0.52
MAE	158.7 mm	0.08	0.2 mm	184.9 km^2	
RMSE	210.5 mm	0.11	0.3 mm	222.7 km^2	
R	0.92	0.98	0.94		

[§] mean_{obs} = basin-average mean observation, mean_{sim} = basin-average mean simulation, Bias = absolute bias, RBias = relative bias (Bias/mean_{obs}), MAE=mean absolute error, RMSE = root mean square error, R = spearman's rank correlation

Performance statistics are reported in Table 8. The VIC-GL model underestimates seasonal peak SWE, with a bias of -130 mm, or -26% of the MSS station mean. Figure 12 shows a spatial comparison of simulated and observed climatological 1971-2000 April 1 SWE. Although the negative bias is evident at most MSS sites, we note that there is no apparent spatial structure to the model residuals. The MSS sites may not be representative of the range of elevation and land cover types found in the much larger grid cell bands, which could account for some of the discrepancy between model and observations. Differences could also be a result of disparities in 'measurement date'; although observations are those for the April 1st survey period, the actual survey date can vary by as much as a week on either side, depending upon site access and other logistical constraints.

A scatterplot of observed and simulated SWE is shown in Figure 13, where we again note the negative bias in the simulated values. Although the difference between band elevation and station elevation does explain some of the discrepancy between simulated and observed values, it does not fully account for the bias (i.e., difference still predominantly negative when *dz*=0; Figure 13b). Despite the bias, both observed and simulated SWE demonstrate a similar relationship of increasing snow accumulation with increasing elevation (Figure 14).

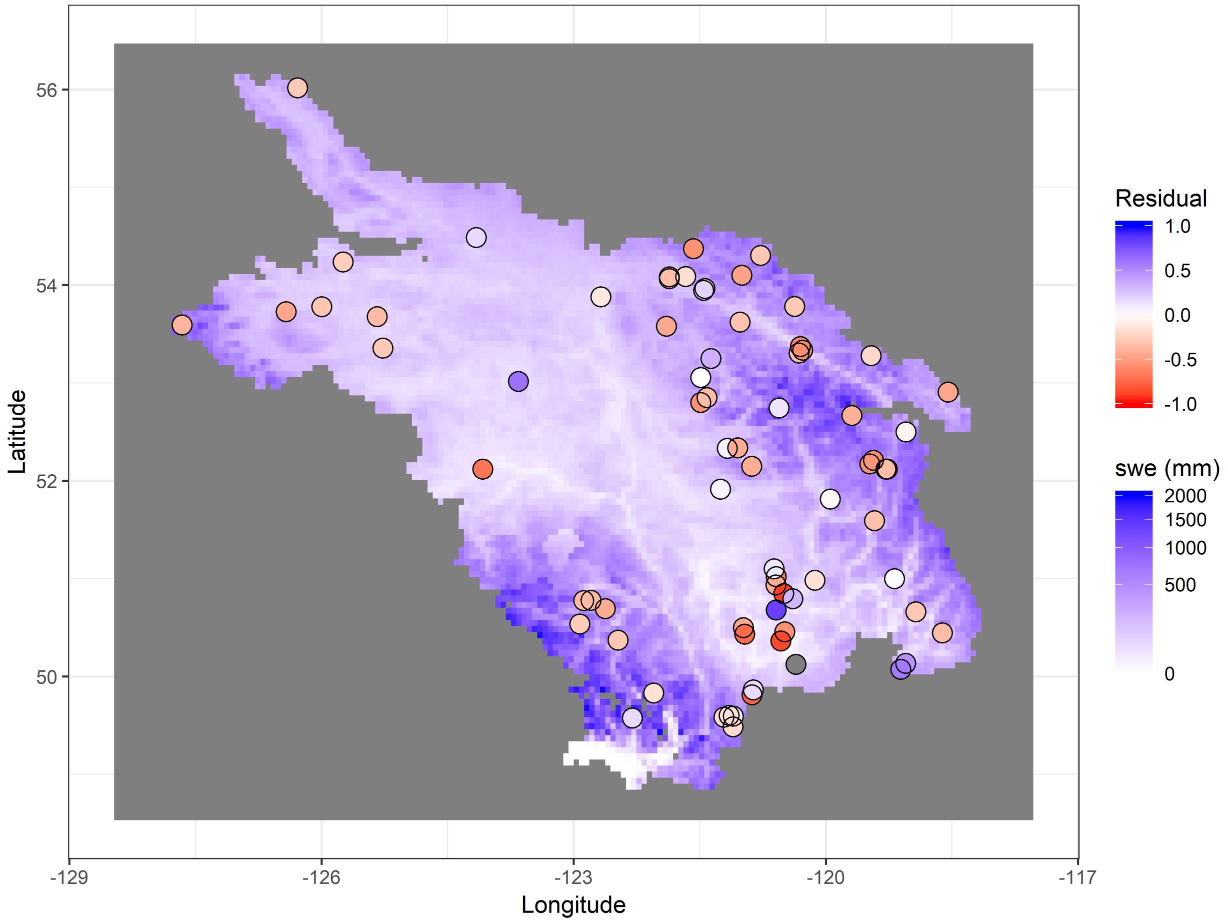

Figure 12. Map of simulated mean April 1 snow water equivalent (1971-2000) compared to observed mean April 1 snow water equivalent at manual snow course locations. Residuals are plotted at each MSS site as fractions ((sim – obs)/obs). Residual values > 1.0 are shown as grey dots.

Inter-annual and decadal variability in snow accumulation is compared using composite time series constructed by averaging SWE observed over all the MSS stations and simulated in the corresponding grid cells. The resultant time series are plotted in Figure 15, where we note a strong correlation between both time series, with a spearman's rank correlation coefficient of 0.92 (significant with $p < 0.01$) (Table 8). Both time series exhibit near-identical inter-annual as well as decadal variability.

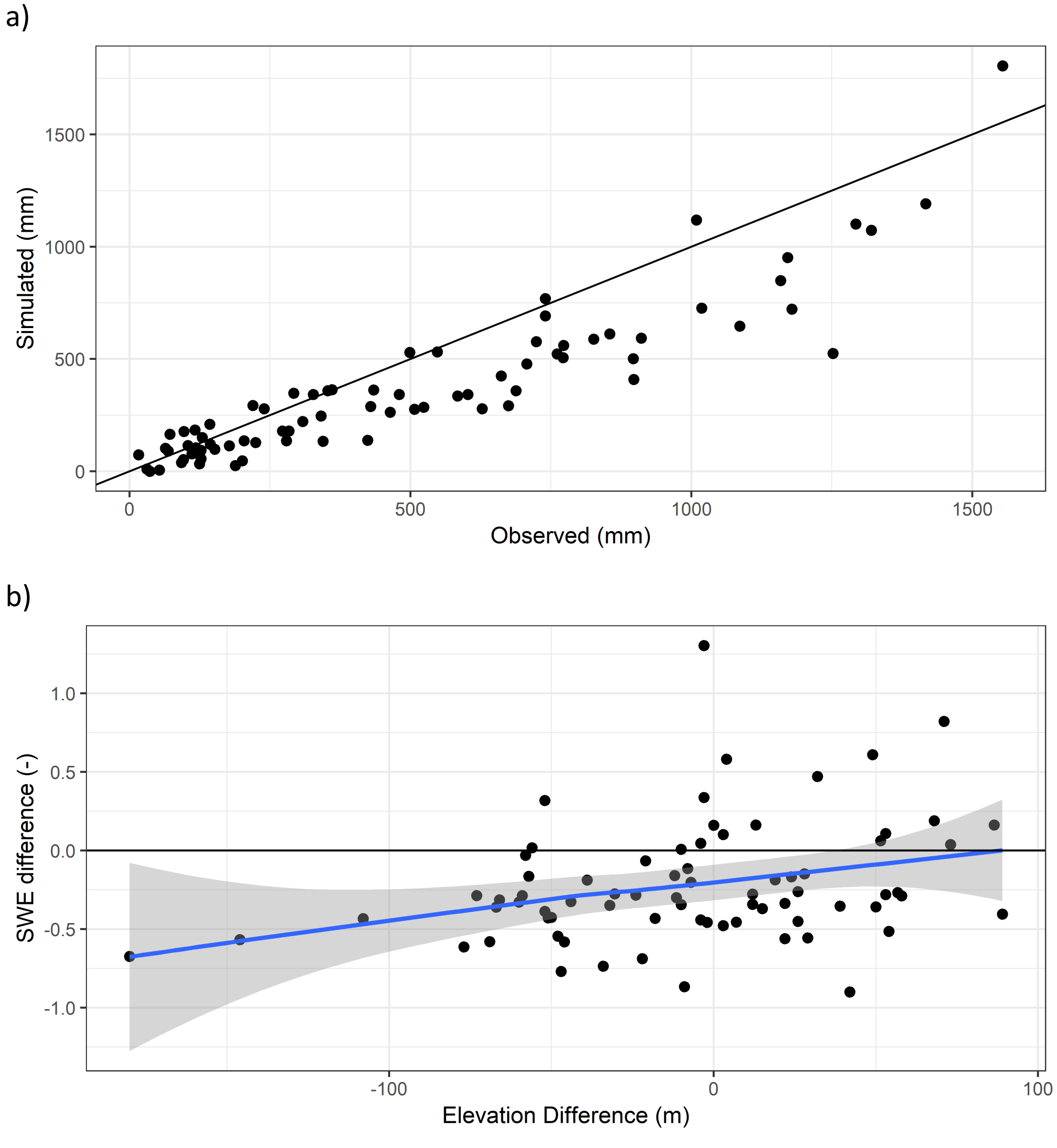

Figure 13. Scatterplot of observed versus simulated climatological (1971-2000) April 1 snow water equivalent. a) Simulated versus observed seasonal peak snow water equivalent with 1:1 line shown for reference, b) difference between simulated and observed SWE as a function of elevation difference between corresponding model grid cell elevation band and MSS station, where solid blue line shows loess smooth and grey shading shows 5-95% confidence interval.

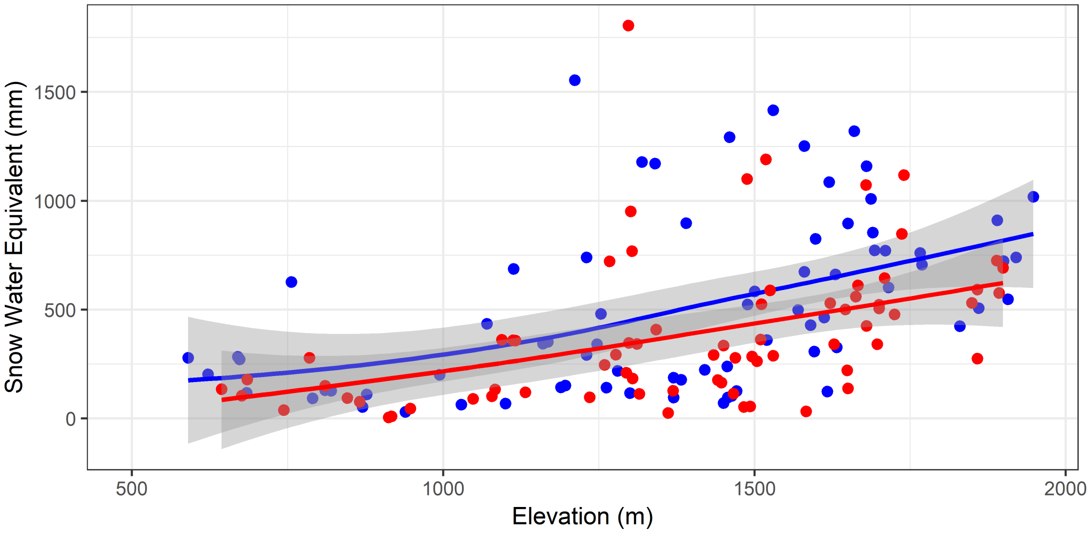

Figure 14. Observed (blue dots) and simulated (red dots) climatological April 1 snow water equivalent as a function of elevation. Red and blue solid lines show loess smooths for observation and simulation, respectively, and grey shading shows the 5-95% confidence intervals.

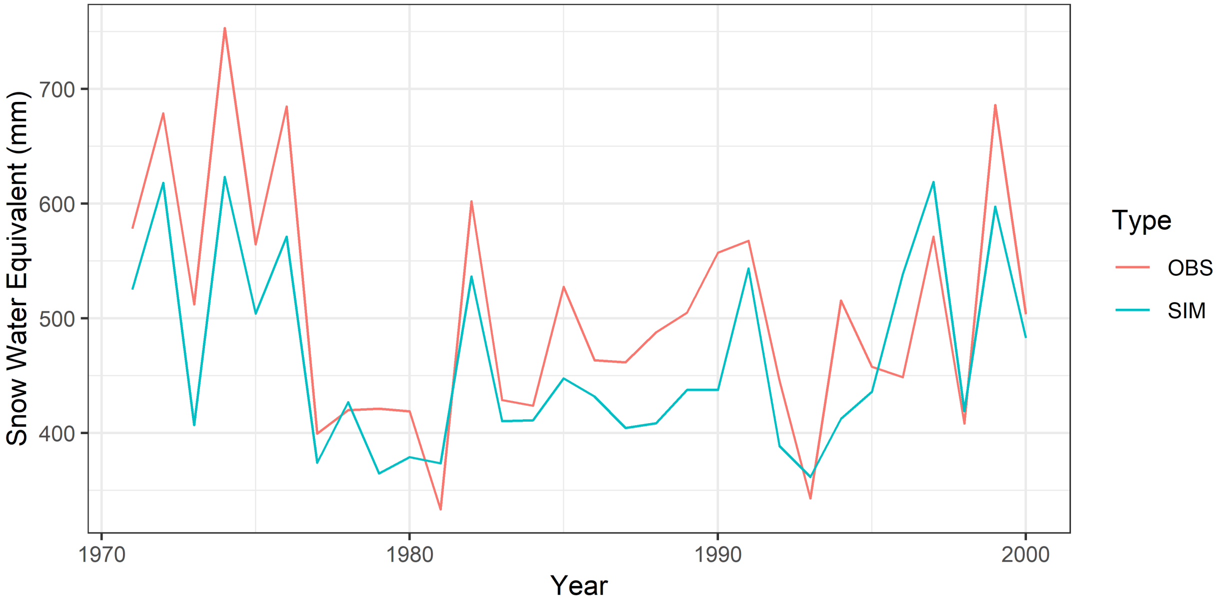

Figure 15. Composite April 1 SWE time series constructed from manual snow survey observations (OBS) and simulated SWE (SIM) from the corresponding VIC-GL model cell and elevation band.

4.2.2 Snow Cover Area

In this section we discuss model performance with respect to snow cover area spatially integrated over the entire Fraser River basin. Observed snow covered area (SCA) is provided by the MODIS/Terra Snow Cover Monthly L3 Global 0.05Deg CMG, Version 6 (MOD10CM) (Hall and Riggs 2015). The MOD10CM product is a satellite-based global estimate of SCA based on the Normalized Difference Snow Index (NDSI). SCA is given as a snow cover fraction for each 0.05° grid. A time series of basin-wide monthly SCA for the Fraser River basin was produced by taking the weighted average of the overlapping 0.05° grids for each month. Area averages were calculated using the `extract` function from the *raster* R package (Hijmans 2016), using normalized weights based on the fraction of each cell within the basin. SCA is compared for the period 2001 to 2010.

The VIC-GL model slightly overestimates SCA, with a bias of 0.08, or 16% (Table 8). The time series of basin-wide monthly SCA, plotted in Figure 16, indicates that simulated seasonal variation matches the observations well, with a spearman's rank correlation of 0.98 ($p < 0.01$) (Table 8). A scatterplot of simulated versus observed monthly SCA, binned by month (Figure 17) shows that the overestimate of SCA occurs during the periods of March-April-May and October-November. This would indicate that the model overestimates the duration and extent of low elevation snow, which would be most sensitive to early melt in the spring and most sensitive to the initiation of accumulation in the late fall. Bias between simulated and observed SCA is negligible during periods of maximum (January-February) and minimum (August-September) snow cover extent.

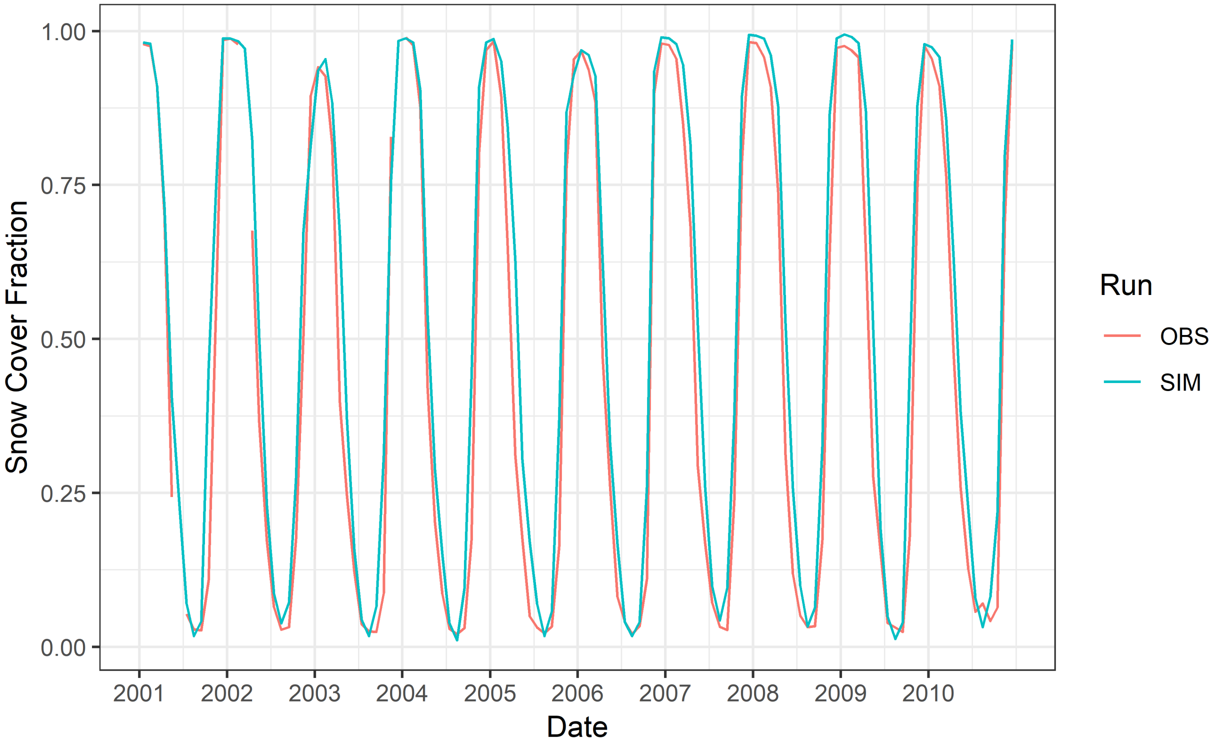

Figure 16. Simulated versus observed monthly snow cover area fraction for the Fraser river basin

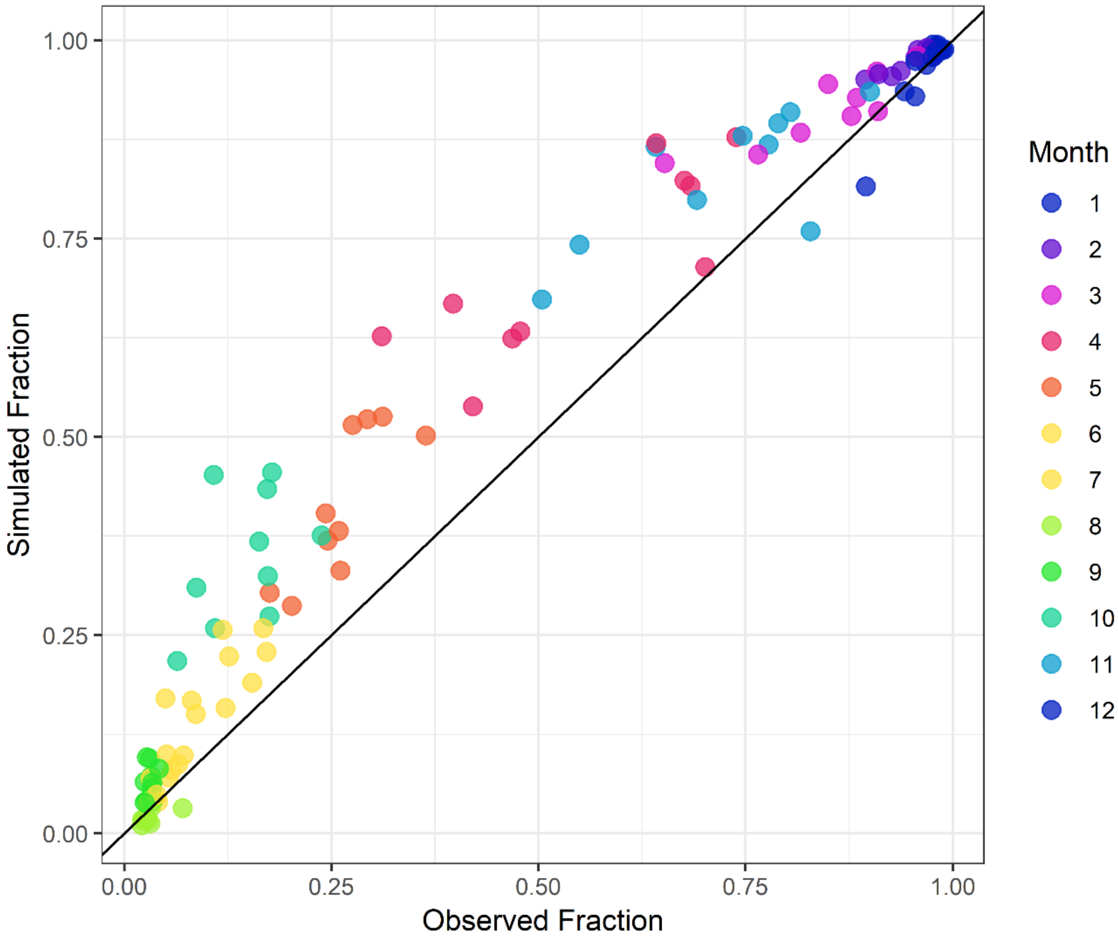

Figure 17. Scatterplot of simulated versus observed basin-wide monthly snow cover area for the period 2001-2010.

Figure 18 shows the seasonal pattern of both the mean in simulated 2001-2010 snow cover in Fraser basin and the difference between seasonal simulated and observed SCA. As anticipated, seasonal snow cover is highest in the winter, when almost the entire basin is covered (exceptions include valley bottoms and the Lower Mainland), and lowest in summer, when only the highest elevations in the Rocky and Coast Mountains contain snow. Snow cover is intermediate during the fall and winter, with a gradient of increasing snow cover with increasing elevation. The differences between simulated and observed SCA again reveal that, where they differ, simulated SCA is predominantly higher than observations in all seasons. This bias is least widespread in winter and summer, when it is generally restricted to the lowest elevations and highest elevations, respectively. The bias is spatially most widespread during the spring and fall, where in spring the bias tends to decrease with increasing elevation but during the fall the bias is more spatially uniform. In general, the bias in SCA is highest when and where snow cover is transitional.

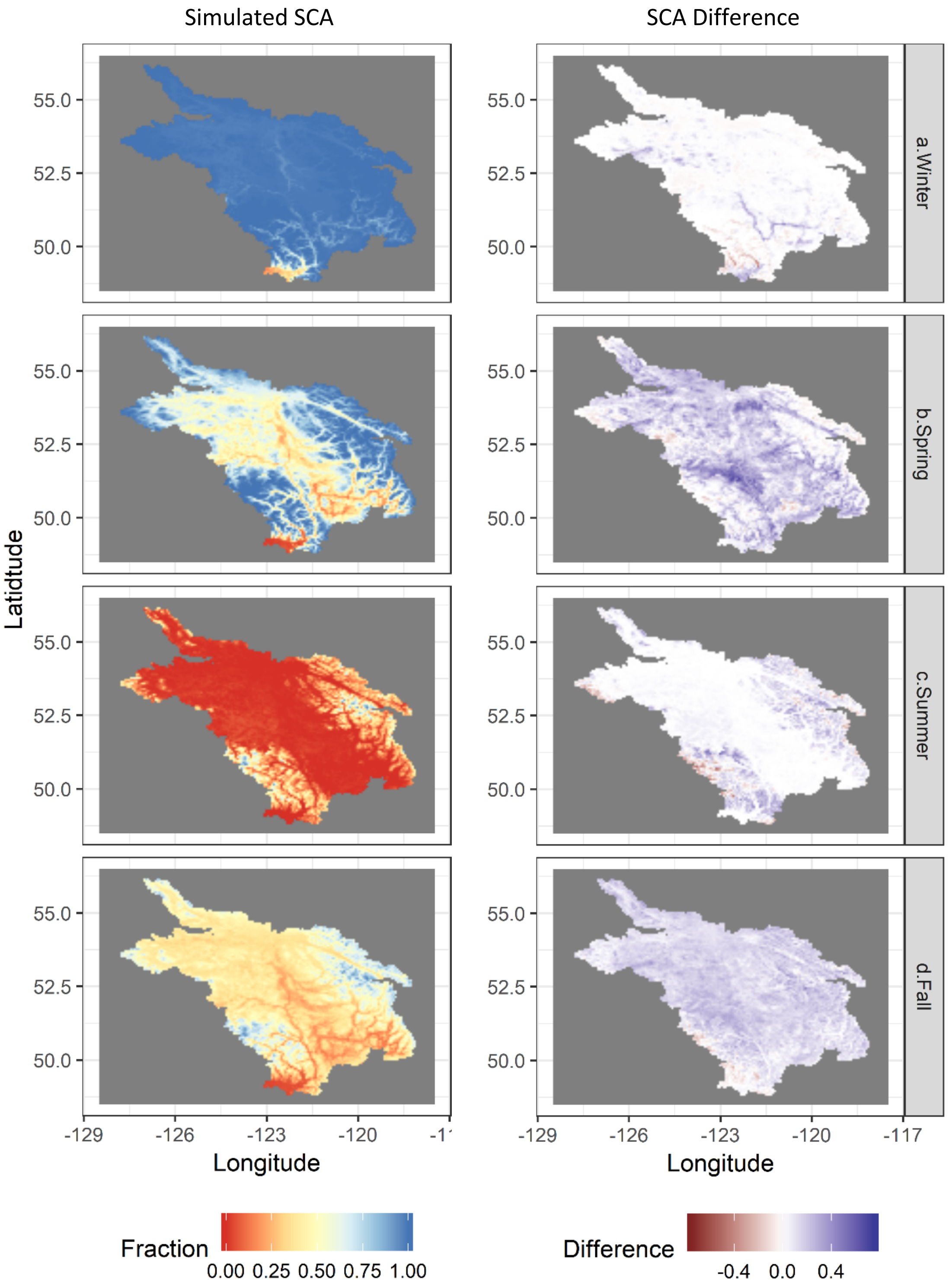

Figure 18. Simulated mean seasonal snow cover area fraction (left column) and difference in seasonal snow cover area fraction between simulation and MODIS observation (right column) for the period 2001 to 2010.

Comparison of SCA and SWE results reveals an apparent paradox where snow accumulation is underestimated but SCA is overestimated. However, SCA is only dependent upon occurrence of snow (if SWE>1 within a hydrologic response unit, then SCA=1) and does not scale with SWE. Therefore, VIC-GL can underestimate SWE and yet overestimate SCA, particularly in regions where snow would normally be discontinuous, such as near the snow line.

4.2.3 Evapotranspiration

In this section, we discuss model performance with respect to evapotranspiration spatially integrated over the entire Fraser River basin. Observed ET data is provided by the LandFlux-EVAL multi-data set synthesis (Mueller et al. 2013). This data set is a monthly global synthesis of land evapotranspiration estimates from 14 global data sets for the period 1989 to 2005. The various products are merged and provided as set of gridded statistics (minimum, maximum, median, mean, 25th percentile, 75th percentile and standard deviation). The original merged product, which has a spatial resolution of 1°, was re-gridded to the spatial resolution of VIC-GL (1/16°) using distance-weighted average remapping using the `remapdis` function in cdo, (CDO 2015). The re-gridded product was then used to calculate basin-wide monthly values of the minimum, maximum and median ET.

Monthly simulated and observed ET (using the ensemble median) are compared over the calibration and validation period in Figure 19. Although simulated ET is biased low with respect to the observed ensemble median, simulated values consistently fall well within the minimum and maximum range of observation ensemble. Basin-wide ET error statistics for the period 1989 to 2005 are summarized in Table 8.

The seasonal pattern of both the mean in simulated ET in Fraser basin and the difference between simulated and the ensemble median observation is shown in Figure 20. VIC-GL shows a reasonable seasonal progression of low ET in the winter (when soil evaporation and transpiration are suppressed by snow and low soil moisture), increasing ET in the spring, maximum ET in the summer (when solar radiation is at a maximum, humidity is at a minimum, and soil is still wet), followed by lower ET in the fall. Unlike the other variables examined, the spatial pattern of simulated ET is affected by parameter artefacts due to sub-basin delineation. Several of the parameters adjusted during model calibration have a direct effect on soil moisture storage and, hence, the amount of water available for soil evaporation and transpiration. As parameters are adjusted by sub-basin, parameter values can exhibit spatial discontinuities across some sub-basin boundaries. Hence, the spatial pattern of ET, particularly during summer, can appear ‘patchy’ (Figure 20).

The spatial pattern of the differences between simulated and the ensemble median observed ET is presented in Figure 20. The negative bias in simulated ET prevails in spring, summer, and fall. However, a clear spatial pattern is only apparent in spring, where bias is small at low elevations (valley bottoms and interior plateau) and largest in the Rocky and Coast Mountains. The difference between observed and simulated ET is mixed during the fall and the spatial pattern is incoherent.

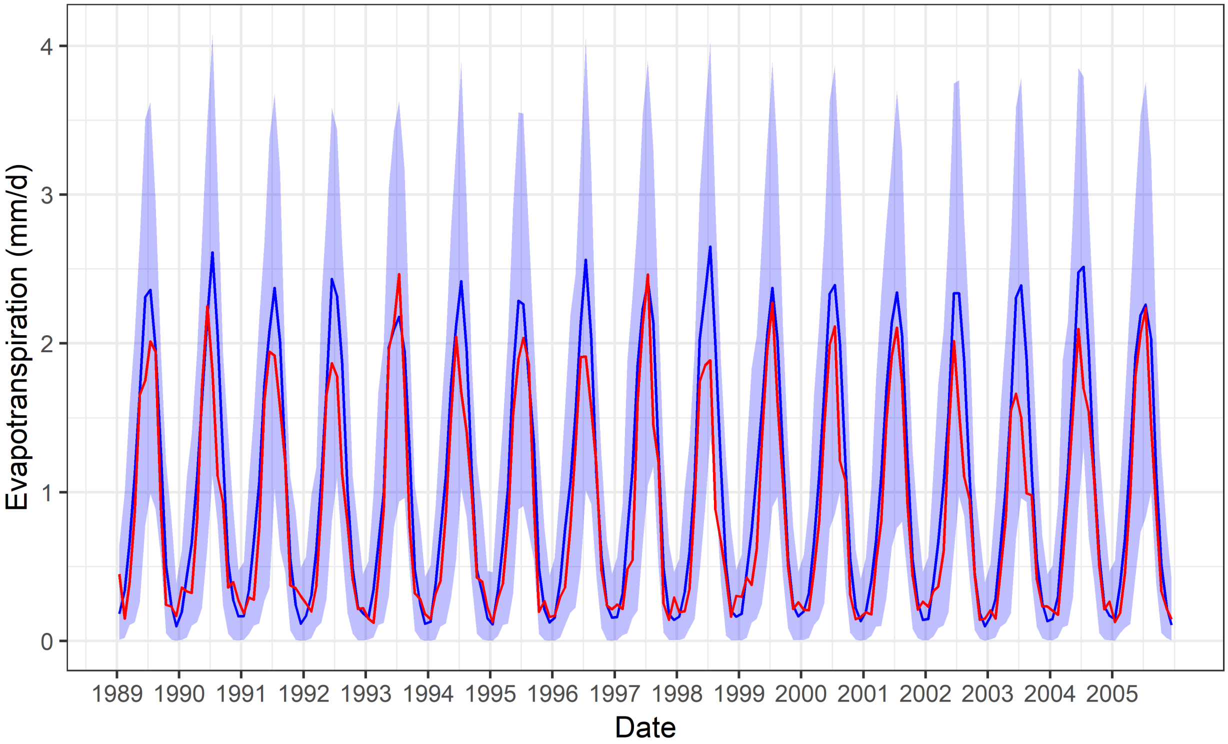

Figure 19. Simulated and observed area-average monthly evapotranspiration for the Fraser basin. Simulated ET shown as the solid red line and observations shown as ensemble with median given by solid blue line and maximum-minimum range by blue shading.

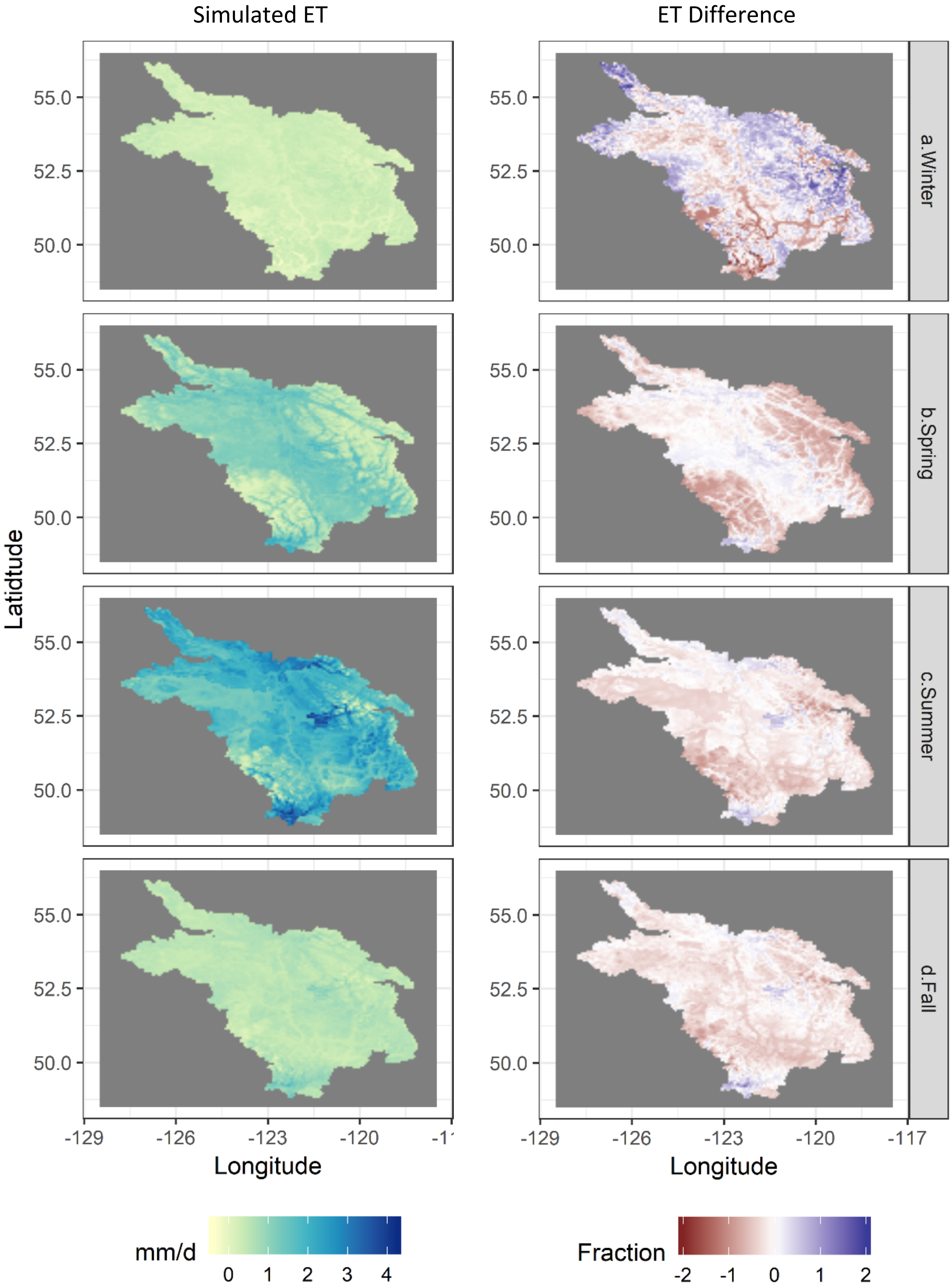

Figure 20. Simulated mean seasonal evapotranspiration and difference in seasonal evapotranspiration between simulation and LandFluxEval ensemble median observation for the period 1989 to 2005.

4.2.4 Glacier Area

This section reviews the performance of the VIC-GL model with respect to simulating glacier area within the basin. As glacier area was not used to constrain model validation, this represents a completely independent assessment of model performance. Validation of glacier area uses glacier inventories produced by Bolch et al. (2010) for the years 1985, 2000 and 2005. Simulated and observed total glacier area in the Fraser River basin is shown in Figure 21 and basin-wide validation statistics are summarized in Table 8. Simulated glacier area has decreased throughout the simulation period and is generally consistent with observed glacier areas (relative bias based on comparison for 1985, 2000 and 2005 is only 1.5% for the basin as a whole).

However, the simulated change in glacier area between 1985 and 2005 is higher than the observed change. The simulated area change is 968.8 km^2 (48.4 km^2/a), which is double the observed change of 476.7 (23.8 km^2/a). Discrepancies between observed and simulated glacier area represents a combination of surface mass balance error in the VIC-GL model and errors in the RGM glacier dynamics model (see section 4.1.4). Due to computational constraints, the sensitivity of glacier area simulation to the specification of the 1945 glacier initial state has not been assessed, but potentially also has an influence on model accuracy.

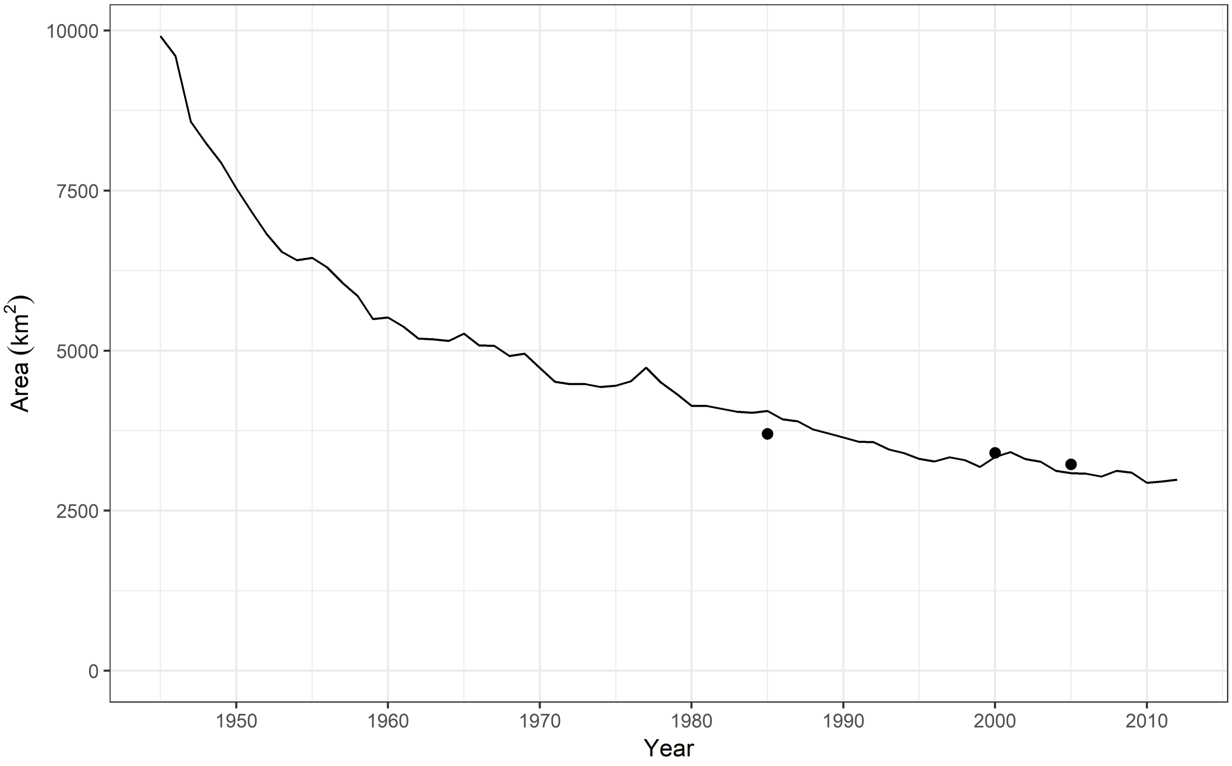

Figure 21. Simulated and observed total glacier area in the Fraser basin. The solid line shows simulated glacier area and the dots represent glacier area observed in the years 1985, 2000 and 2005.

5 Experimental Design

5.1 Climate Forcing

Hydrologic projections employed an ensemble modelling approach, whereby the hydrology model was forced with meteorological data statistically downscaled from climate experiments generated using a range of different global climate models (GCMs) forced by two emissions scenarios. The ensemble uses climate data produced as part of the World Climate Research Programme (WCRP) Coupled Model Intercomparison Project Phase 5 (CMIP5) (Taylor et al. 2012). The CMIP5 experiments are based on emissions specified by Representative Concentration Pathway (RCP) scenarios, which are a set of four greenhouse concentrations trajectories developed for the climate modeling community as a basis for long-term and near-term modeling experiments. The RCPs are consistent with a wide range of possible changes in future anthropogenic greenhouse gas (GHG) emissions and aim to represent their atmospheric concentrations. We have utilized climate projections from two such scenarios, RCP 8.5, and RCP 4.5. Emissions in RCP 4.5 peak around 2040 then decline and in RCP 8.5 emissions continue to rise throughout the 21st century. See van Vuuren et al. 2011 for description of the RCP scenarios.

To reduce computational time and ease interpretation of results, output from a subset of six (6) GCMs of all the available CMIP5 models has been used. Using all available runs (some GCMs were used to produce multiple runs per scenario), the resulting ensemble consists of 31 climate projections (16 each for RCP4.5 and RCP8.5, respectively), which are summarized in Table 1. The process of GCM selection entails selecting the subset of GCMs that best represent the overall spread of the full CMIP5 ensemble (Cannon 2015). This ensemble design explicitly assesses the uncertainty in future projections due to a range of greenhouse gas emissions and uncertainty due to differences in GCM output. Interpretation of the climate projections and derived hydrologic projections is based on the statistical paradigm that the individual projections are statistically indistinguishable (Annan and Hargreaves 2010; Knutti et al. 2010). In such a case, each ensemble member is considered indistinguishable from all possible outcomes of the earth's chaotic processes (Knutti et al. 2010), and the outcome of no one individual projection is considered more probable than any other.

The global climate response to a prescribed emission scenario generated by a GCM is of too coarse a spatial resolution to be used directly in obtaining a hydrologic response for the study area. The output from a GCM does not typically contain sufficient regional detail on the change in climate, which is affected by such factors as local topography, orography, and coastal effects. Therefore, downscaling the global climate signal into a regional climate signal is a necessary intermediate step. All projections have been downscaled with the Bias Correction/Constructed Analogues with Quantile mapping reordering (BCCAQ). BCCAQ is a hybrid method that combines results from bias-corrected constructed analogs (BCCA) (Maurer et al. 2010) and quantile mapping (QMAP) (Gudmundsson et al. 2012). BCCA obtains spatial information from a linear combination of historical analogues for daily large-scale fields, avoiding the need for monthly aggregates. QMAP applies quantile mapping to daily climate model outputs that have been interpolated to the high-resolution grid using the climate imprint method of Hunter and Meentemeyer (2005). For more information on BCCAQ, see Werner and Cannon (2016).

Table 9. Global climate experiments used in hydrologic projection ensemble

Model ID	Institution	Run Numbers	
		RCP45	RCP85
ACCESS1-1	Commonwealth Scientific and Industrial Research Organisation and Bureau of Meteorology, Australia	1	1
CanESM2	Canadian Centre for Climate Modelling and Analysis, Canada	5	5
CCSM4	National Center for Atmospheric Research, United States	2	2
CNRM-CM5	Centre National de Recherches Météorologiques and Centre Européen de Recherche et Formation Avancée en Calcul Scientifique, France	1	1
HadGEM2-ES	Met Office Hadley Centre, United Kingdom	4	4
MPI-ESM-LR	Max Planck Institute for Meteorology, Germany	3	3

5.2 Model Initialization

To start a model simulation, the model must be initialized be specifying values for all state variables (such as snow depth, soil moisture, etc.). Model spin-up is then the time taken for the hydrology model to reach a state of statistical equilibrium under the applied forcing. When running a model, one can employ either a ‘cold start’ or a ‘warm start’. A cold start usually occurs when a model is initialized and needs to be spun up; a warm start is a restart of a model, which is used to reduce spin-up time. Prior to the introduction of the glacier dynamics component of the model, VIC was initialized with default values for all fields and run from a cold start with a five-year spin-up period. This was an acceptable practice as many of the state variables are highly seasonal and reach statistical equilibrium after only one year. Other more persistent processes, such as soil moisture, can take several years.

With the inclusion of glacier dynamics into the upgraded VIC-GL model, initialization and spin-up become more complicated due to the decadal response time of glaciers to climatic variability. As all projections are designed to begin in 1945, a fully initialized and spun-up glacier state is required for this year for all basins with glacier area greater than 1 km^2. The glacier state must be provided as values of glacier depth on a computational grid with a spatial resolution of 100-m (e.g., see Figure 22). Glacier depth is the difference between surface topography and an estimate of sub-glacial topography (Clarke et al. 2013). As no observations of glacial depth exist for 1945, an initial glacier state must be estimated. The process used is a combined initialization and spin-up process, which is intended to give a plausible description of the spatial distribution of glacier depth for the year 1945. The process has three main steps: 1) derive a climatological surface mass balance for 1901-1930, 2) derive and initial ‘first- guess’ glacier state (glacier depth) from 500-year steady state run, and 3) derive final glacier state from 45-year spin-up.

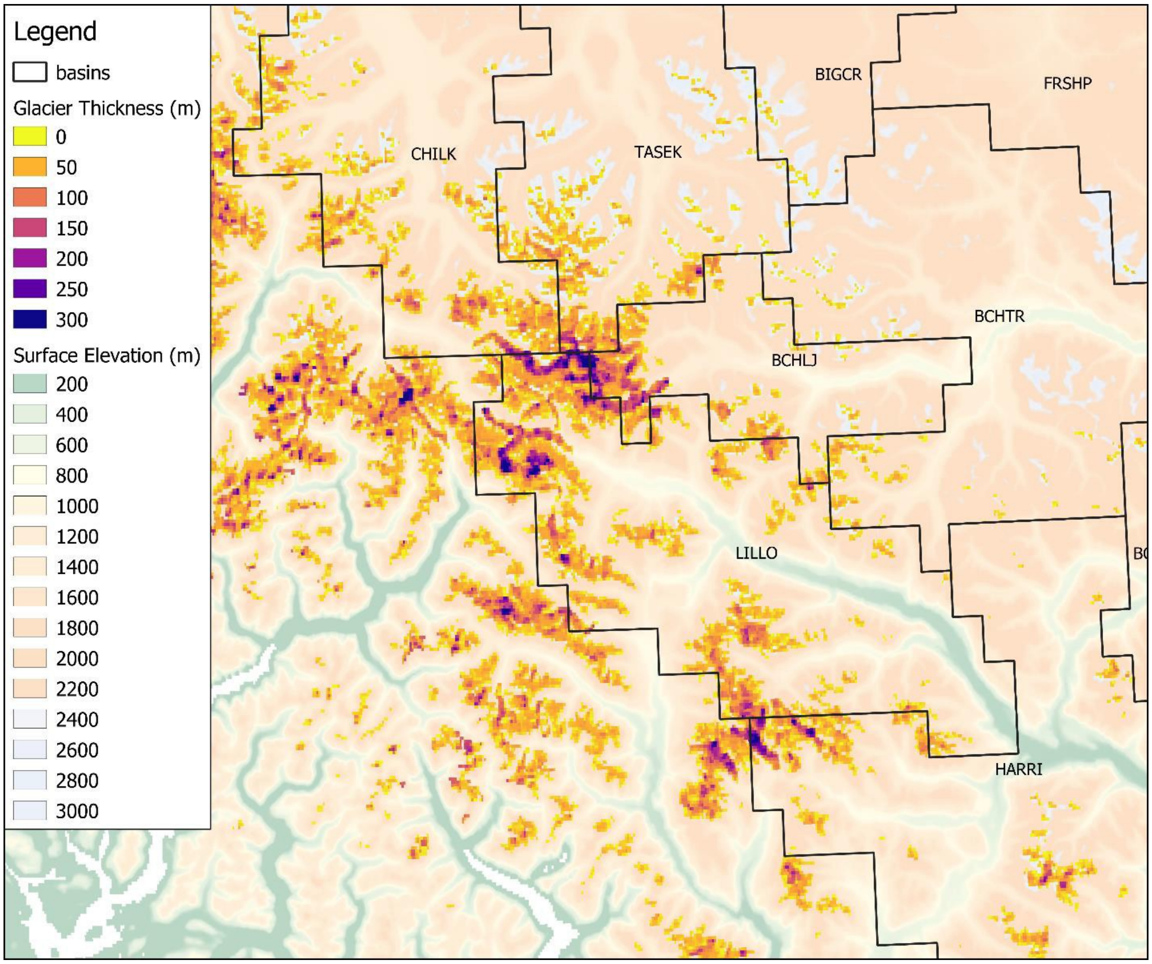

Figure 22. Glacier thickness circa 2005 for south coast region of Fraser study domain. Glacier thickness is estimated as surface topography minus bed topography (see text for details).

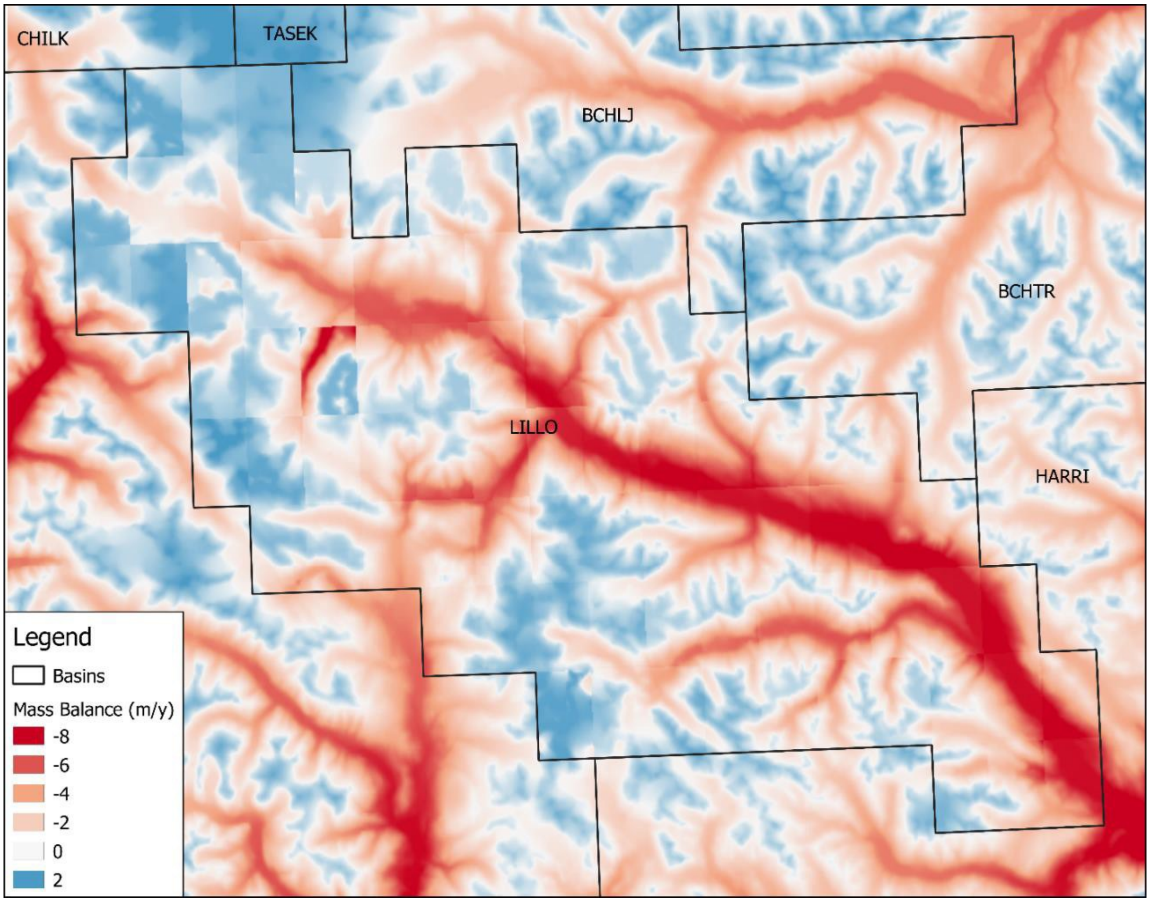

Figure 23. Surface glacier mass balance climatology (1901-1930) for the Lillooet sub-basin and surrounding region

Step one is to run the fully coupled VIC-GL model for the period 1901 to 1930, which is used to derive and average 30-year glacier surface mass balance. The surface mass balance is defined as the annual difference between snow accumulation and snow and glacier melt. An example of such a surface mass balance field is given in Figure 23. This turn-of-the-century climatological mass balance is subsequently used in step two to run the glacier dynamics model offline (i.e., uncoupled) in steady state (constant mass balance forcing) for a 500-year period. This step starts with a bare surface topography (i.e., no glaciers) and uses the 500-year period to estimate an initial glacier surface on the landscape to a depth and at locations consistent with the supplied mass balance field. As a steady 30-year average mass balance does not realistically portray actual historical climate variability, a third step incorporates a final spin-up period. This spin-up period uses the fully coupled model to run transient simulations (i.e., climate and mass balance change through time) from 1901 to 1945 and commences with the initialized glacier surface produced during step two. The purpose of this spin-up is to 'fine-tune' the glacier surface so that the glacier state more accurately reflects climate variability experienced in the final decades prior to 1945. All coupled VICGL simulations (steps one and three) are forced using the NOAA-CIRES 20th century reanalysis version 2c (Compo et al. 2011).

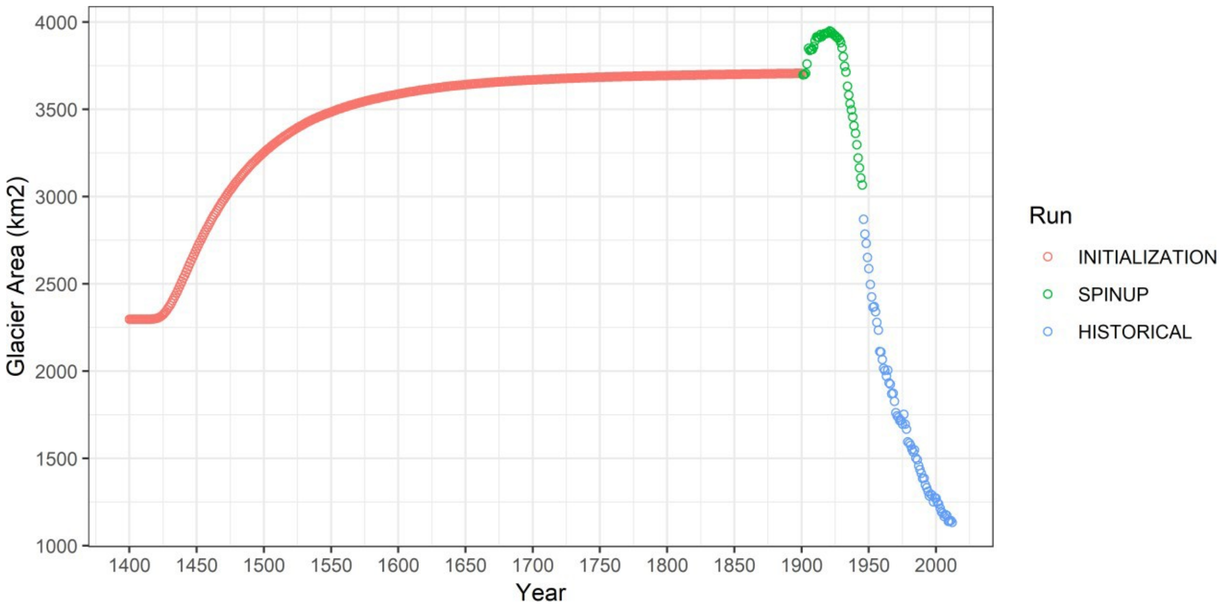

Figure 24. Simulated glacier area for the Lillooet sub-basin during glacier initialization, spin-up and historical simulation, represented as a single time series

The evolution of glacier area during the initialization and spin-up process (steps two and three) for the Lillooet sub-basin is shown in Figure 24. Under steady-state surface mass balance forcing, glacier area asymptotically approaches 3700 km^2 after 500 years. During the spin-up period there is a rapid increase in glacier area for 25 years (1901 to 1925) followed by a decreasing trend in the final decades leading up to 1945. The final estimate glacier area in 1945 is ~3100 km^2. In addition, Figure 24 shows the continuing decline in glacier area from 1945 to 2012 as simulated using the observation-driven historical run.

6 References

Adam, J. C., and D. P. Lettenmaier, 2003: Adjustment of global gridded precipitation for systematic bias. *J. Geophys. Res.-Atmospheres*, **108**, https://doi.org/4257 10.1029/2002jd002499.

Adam, J. C., E. A. Clark, D. P. Lettenmaier, and E. F. Wood, 2006: Correction of Global Precipitation Products for Orographic Effects. *J. Clim.*, **19**, 15–38, https://doi.org/Article.

Baret, F., M. Weiss, R. Lacaze, F. Camacho, H. Makhmara, P. Pacholcyzk, and B. Smets, 2013: GEOV1: LAI and FAPAR essential climate variables and FCOVER global time series capitalizing over existing products. Part1: Principles of development and production. *Remote Sens. Environ.*, **137**, 299–309, https://doi.org/10.1016/j.rse.2012.12.027.

Barnett, T. P., and Coauthors, 2008: Human-Induced Changes in the Hydrology of the Western United States. *Science*, **319**, 1080–1083, https://doi.org/10.1126/science.1152538.

Batjes, N. H., 1995: *A homogenized soil data file for global environmental research: A subset of FAO, ISRIC and NRCS profiles (Version 1.0)*. International Soil Reference and Information Centre,.

Bolch, T., B. Menounos, and R. Wheate, 2010: Landsat-based inventory of glaciers in western Canada, 1985–2005. *Remote Sens. Environ.*, **114**, 127–137, https://doi.org/10.1016/j.rse.2009.08.015.

Bonfils, C., and Coauthors, 2008: Detection and Attribution of Temperature Changes in the Mountainous Western United States. *J. Clim.*, **21**, 6404–6424, https://doi.org/10.1175/2008JCLI2397.1.

Box, G. E. P., and D. R. Cox, 1964: An Analysis of Transformations. *J. R. Stat. Soc. Ser. B Methodol.*, **26**, 211–252.

Camacho, F., J. Cernicharo, R. Lacaze, F. Baret, and M. Weiss, 2013: GEOV1: LAI, FAPAR essential climate variables and FCOVER global time series capitalizing over existing products. Part 2: Validation and intercomparison with reference products. *Remote Sens. Environ.*, **137**, 310–329, https://doi.org/10.1016/j.rse.2013.02.030.

Cannon, A. J., 2015: Selecting GCM Scenarios that Span the Range of Changes in a Multimodel Ensemble: Application to CMIP5 Climate Extremes Indices. *J. Clim.*, **28**, 1260–1267, https://doi.org/10.1175/JCLI-D-14-00636.1.

Cavazzuti, M., 2013: *Optimization Methods - From Theory to Design*. Springer-Verlag, 262 pp.

CDO, 2015: *Climate Data Operators*.

Cherkauer, K. A., L. C. Bowling, and D. P. Lettenmaier, 2003: Variable infiltration capacity cold land process model updates. *Glob. Planet. Change*, **38**, 151–159, https://doi.org/10.1016/S0921-8181(03)00025-0.

Clarke, G. K. C., F. S. Anslow, A. H. Jarosch, V. Radić, B. Menounos, T. Bolch, and E. Berthier, 2013: Ice Volume and Subglacial Topography for Western Canadian Glaciers from Mass Balance Fields, Thinning Rates, and a Bed Stress Model. *J. Clim.*, **26**, 4282–4303, https://doi.org/10.1175/JCLI-D-12-00513.1.

——, A. H. Jarosch, F. S. Anslow, V. Radić, and B. Menounos, 2015a: Projected deglaciation of western Canada in the twenty-first century. *Nat. Geosci.*, **8**, 372–377, https://doi.org/10.1038/ngeo2407.

——, ——, ——, ——, and ——, 2015b: Projected deglaciation of western Canada in the twenty-first century. *Nat. Geosci.*, **8**, 372–377, https://doi.org/10.1038/ngeo2407.

Climate Prediction Centre NOAA, 2015: Cold and warm episodes by season. *Hist. El Nino Nina Episodes 1950-Present*,. http://www.cpc.ncep.noaa.gov/products/analysis_monitoring/ensostuff/ensoyears.shtml (Accessed June 2, 2017).

Curry, C. L., S. U. Islam, F. W. Zwiers, and S. J. Déry, 2019: Atmospheric Rivers Increase Future Flood Risk in Western Canada's Largest Pacific River. *Geophys. Res. Lett.*, **46**, 1651–1661, https://doi.org/10.1029/2018GL080720.

Dai, A., 2013: Increasing drought under global warming in observations and models. *Nat. Clim. Change*, **3**, 52–58, https://doi.org/10.1038/nclimate1633.

Danielson, J. J., and D. B. Gesch, 2011: *Global Multi-resolution Terrain Elevation Data 2010 (GMTED2010)*. U.S. Geological Survey, http://pubs.usgs.gov/of/2011/1073/pdf/of2011-1073.pdf (Accessed November 2, 2015).

Deb, K., A. Pratap, S. Agarwal, and T. Meyarivan, 2002: A fast and elitist multiobjective genetic algorithm: NSGA-II. *IEEE Trans. Evol. Comput.*, **6**, 182–197, https://doi.org/10.1109/4235.996017.

Demaria, E. M., B. Nijssen, and T. Wagener, 2007: Monte Carlo sensitivity analysis of land surface parameters using the Variable Infiltration Capacity model. *J. Geophys. Res.-Atmospheres*, **112**, https://doi.org/D11113 10.1029/2006jd007534.

FAO-UNESCO, 1995: Digital soil map of the world.

Global Soil Data Task, 2014: Global Soil Data Products CD-ROM Contents (IGBP-DIS). *ORNL DAAC*, https://doi.org/10.3334/ORNLDAAC/565.

Gupta, H. V., H. Kling, K. K. Yilmaz, and G. F. Martinez, 2009: Decomposition of the mean squared error and NSE performance criteria: Implications for improving hydrological modelling. *J. Hydrol.*, **377**, 80–91, https://doi.org/10.1016/j.jhydrol.2009.08.003.

Hall, D. K., and G. A. Riggs, 2015: MODIS/Terra Snow Cover Monthly L3 Global 0.05Deg CMG, Version 6. http://dx.doi.org/10.5067/MODIS/MOD10CM.006.

Hamlet, A. F., and D. P. Lettenmaier, 2007: Effects of 20th century warming and climate variability on flood risk in the western U.S. *Water Resour. Res.*, **43**, W06427, https://doi.org/10.1029/2006WR005099.

Hijmans, R. J., 2016: *raster: Geographic Data Analysis and Modeling*.

Hirabayashi, Y., R. Mahendran, S. Koirala, L. Konoshima, D. Yamazaki, S. Watanabe, H. Kim, and S. Kanae, 2013: Global flood risk under climate change. *Nat. Clim. Change*, **3**, 816–821, https://doi.org/10.1038/nclimate1911.

Hunter, R. D., and R. K. Meentemeyer, 2005: Climatologically Aided Mapping of Daily Precipitation and Temperature. *J. Appl. Meteorol.*, **44**, 1501–1510, https://doi.org/10.1175/JAM2295.1.

Islam, S. ul, S. J. Déry, and A. T. Werner, 2017: Future Climate Change Impacts on Snow and Water Resources of the Fraser River Basin, British Columbia. *J. Hydrometeorol.*, **18**, 473–496, https://doi.org/10.1175/JHM-D-16-0012.1.

Jarosch, A. H., C. G. Schoof, and F. S. Anslow, 2013: Restoring mass conservation to shallow ice flow models over complex terrain. *The Cryosphere*, **7**, 229–240, https://doi.org/10.5194/tc-7-229-2013.

Kelliher, F. M., R. Leuning, M. R. Raupach, and E.-D. Schulze, 1995: Maximum conductances for evaporation from global vegetation types. *Agric. For. Meteorol.*, **73**, 1–16, https://doi.org/10.1016/0168-1923(94)02178-M.

Klemeš, V., 1986: Operational testing of hydrological simulation models. *Hydrol. Sci. J.*, **31**, 13–24, https://doi.org/10.1080/02626668609491024.

Liang, X., D. P. Lettenmaier, E. F. Wood, and S. J. Burges, 1994: A simple hydrologically based model of land-surface water and energy fluxes for general-circulation models. *J. Geophys. Res.-Atmospheres*, **99**, 14415–14428, https://doi.org/10.1029/94JD00483.

Liang, X., E. F. Wood, and D. P. Lettenmaier, 1996: Surface soil moisture parameterization of the VIC-2L model: Evaluation and modification. *Glob. Planet. Change*, **13**, 195–206, https://doi.org/10.1016/0921-8181(95)00046-1.

Lohmann, D., E. Raschke, B. Nijssen, and D. P. Lettenmaier, 1998: Regional scale hydrology: II. Application of the VIC-2L model to the Weser River, Germany. *Hydrol. Sci. J.-J. Sci. Hydrol.*, **43**, 143–158, https://doi.org/10.1080/02626669809492108.

Mersmann, O., 2014: *mco: Multiple Criteria Optimization Algorithms and Related Functions*.

Milly, P. C. D., J. Betancourt, M. Falkenmark, R. M. Hirsch, Z. W. Kundzewicz, D. P. Lettenmaier, and R. J. Stouffer, 2008: Stationarity Is Dead: Whither Water Management? *Science*, **319**, 573–574, https://doi.org/10.1126/science.1151915.

Moss, R. H., and Coauthors, 2010: The next generation of scenarios for climate change research and assessment. *Nature*, **463**, 747–756, https://doi.org/10.1038/nature08823.

Mueller, B., and Coauthors, 2013: Benchmark products for land evapotranspiration: LandFlux-EVAL multi-data set synthesis. *Hydrol Earth Syst Sci*, **17**, 3707–3720, https://doi.org/10.5194/hess-17-3707-2013.

Nash, J. E., and J. V. Sutcliffe, 1970: River flow forecasting through conceptual models. Part I - discussion of principles. *J. Hydrol.*, **10**, 282–290.

Nychka, D., R. Furrer, J. Paige, and S. Sain, 2017: *fields: Tools for Spatial Data*.

Peterson, T. C., and Coauthors, 2013: Monitoring and Understanding Changes in Heat Waves, Cold Waves, Floods, and Droughts in the United States: State of Knowledge. *Bull. Am. Meteorol. Soc.*, **94**, 821–834, https://doi.org/10.1175/BAMS-D-12-00066.1.

Pfeffer, W. T., and Coauthors, 2014: The Randolph Glacier Inventory: A globally complete inventory of glaciers. *J. Glaciol.*, **221**, 537–552, https://doi.org/10.3189/2014JoG13J176.

Pierce, D. W., and Coauthors, 2008: Attribution of declining Western U.S. snowpack to human effects. *J. Clim.*, **21**, 6425–6444, https://doi.org/10.1175/2008JCLI2405.1.

Produced by Natural Resources Canada/ The Canada Centre for Mapping and Earth Observation (NRCan/CCMEO), United States Geological Survey (USGS), Insituto Nacional de Estadística y Geografía (INEGI), Comisión Nacional para el Conocimiento y Uso de la Biodiversidad (CONABIO), and Comisión Nacional Forestal (CONAFOR), 2013: 2010 North American Land Cover at 250 m spatial resolution.

R Core Team, 2016: *R: A Language and Environment for Statistical Computing*. R Foundation for Statistical Computing,.

Rodenhuis, D., K. E. Bennett, A. T. Werner, T. Q. Murdock, and D. Bronaugh, 2009: *Climate overview 2007: Hydro-climatology and future climate impacts in British Columbia*. Pacific Climate Impacts Consortium,.

Schiefer, E., B. Menounos, and R. Wheate, 2007: Recent volume loss of British Columbian glaciers, Canada. *Geophys. Res. Lett.*, **34**, L16503, https://doi.org/10.1029/2007GL030780.

Schnorbus, M., 2016: *VIC Second-Generation Vegetation and Topography Parameterization*. Pacific Climate Impacts Consortium,.

——, 2018: *VIC-Glacier (VIC-GL) Description of VIC Model Changes and Upgrades*. Pacific Climate Impacts Consortium, University of Victoria,.

——, K. Bennett, and A. Werner, 2010: *Quantifying the water resource impacts of mountain pine beetle and associated salvage harvest operations across a range of watershed scales: Hydrologic modelling of the Fraser River basin.* Canadian Forest Service, Pacific Forestry Centre, http://www.cfs.nrcan.gc.ca/pubwarehouse/pdfs/31207.pdf.

——, A. Werner, and K. Bennett, 2014: Impacts of climate change in three hydrologic regimes in British Columbia, Canada. *Hydrol. Process.*, **28**, 1170–1189, https://doi.org/10.1002/hyp.9661.

Sheffield, J., and E. F. Wood, 2008: Projected changes in drought occurrence under future global warming from multi-model, multi-scenario, IPCC AR4 simulations. *Clim. Dyn.*, **31**, 79–105, https://doi.org/10.1007/s00382-007-0340-z.

Shrestha, R. R., M. A. Schnorbus, A. T. Werner, and A. J. Berland, 2012: Modelling spatial and temporal variability of hydrologic impacts of climate change in the Fraser River basin, British Columbia, Canada. *Hydrol. Process.*, **26**, 1840–1860, https://doi.org/10.1002/hyp.9283.

——, ——, and D. L. Peters, 2016: Assessment of a hydrologic model's reliability in simulating flow regime alterations in a changing climate. *Hydrol. Process.*, **30**, 2628–2643, https://doi.org/10.1002/hyp.10812.

Simard, M., N. Pinto, J. B. Fisher, and A. Baccini, 2011: Mapping forest canopy height globally with spaceborne lidar. *J. Geophys. Res. Biogeosciences*, **116**, G04021, https://doi.org/10.1029/2011JG001708.

Sorooshian, S., and J. A. Dracup, 1980: Stochastic parameter estimation procedures for hydrologic rainfall-runoff models: Correlated and heteroscedastic error cases. *Water Resour. Res.*, **16**, 430–442, https://doi.org/10.1029/WR016i002p00430.

——, V. K. Gupta, and J. L. Fulton, 1983: Evaluation of Maximum Likelihood Parameter estimation techniques for conceptual rainfall-runoff models: Influence of calibration data variability and length on model credibility. *Water Resour. Res.*, **19**, 251–259, https://doi.org/10.1029/WR019i001p00251.

Taylor, K. E., R. J. Stouffer, and G. A. Meehl, 2012: An Overview of CMIP5 and the Experiment Design. *Bull. Am. Meteorol. Soc.*, **93**, 485–498, https://doi.org/10.1175/BAMS-D-11-00094.1.

Todini, E., 1996: The ARNO rainfall—runoff model. *J. Hydrol.*, **175**, 339–382, https://doi.org/10.1016/S0022-1694(96)80016-3.

van Vuuren, D. P., and Coauthors, 2011: The representative concentration pathways: an overview. *Clim. Change*, **109**, 5–31, https://doi.org/10.1007/s10584-011-0148-z.

Werner, A. T., M. A. Schnorbus, R. R. Shrestha, and H. D. Eckstrand, 2013: Spatial and Temporal Change in the Hydro-Climatology of the Canadian Portion of the Columbia River Basin under Multiple Emissions Scenarios. *Atmosphere-Ocean*, **51**, 357–379, https://doi.org/10.1080/07055900.2013.821400.

——, ——, ——, A. J. Cannon, F. W. Zwiers, G. Dayon, and F. Anslow, 2019: A long-term, temporally consistent, gridded daily meteorological dataset for northwestern North America. *Sci. Data*, **6**, 180299.

Zhao, J., and B. K. Bose, 2002: Evaluation of membership functions for fuzzy logic controlled induction motor drive. *IECON 02 [Industrial Electronics Society, IEEE 2002 28th Annual Conference]*, Vol. 1 of, IECON 02 [Industrial Electronics Society, IEEE 2002 28th Annual Conference], Sevilla, Spain, IEEE, 229–234 vol.1.

Appendix A – Tables

Table A1. Peace River sub-basins for the VICGL model

Basin Code	Sub-basin Name	Area (km^2)	Glacier Area (km^2) §
ARNT7	AKIE RIVER NEAR 760M CONTOUR	1859	46
BRBAC	BLUEBERRY RIVER BELOW AITKEN CREEK	1779	0
BRNFS	BEATTON RIVER NEAR FORT ST. JOHN	14699	0
FRAAR	FINLAY RIVER ABOVE AKIE RIVER	14786	42
GRACC	GRAHAM RIVER ABOVE COLT CREEK	2249	0
HERNN	HEART RIVER NEAR NAMPA, AB	2249	0
HRAGR	HALFWAY RIVER ABOVE GRAHAM RIVER	4116	0
HRNFC	HALFWAY RIVER NEAR FARRELL CREEK	3256	0
IRASR	INGENEKA RIVER ABOVE SWANNELL RIVER	4322	<1
KIRNF	KISKATINAW RIVER NEAR FARMINGTON	3524	0
KWRNW	KWADACHA RIVER NEAR WARE	2697	130
LSRNG	LITTLE SMOKY RIVER NEAR GUY, AB	10996	0
MRAGC	MESILINKA RIVER ABOVE GOPHERHOLE CREEK	3172	5
MRAWR	MURRAY RIVER ABOVE WOLVERINE RIVER	2520	26
MRNFS	MOBERLY RIVER NEAR FORT ST. JOHN	1390	0
MRNTM	MURRAY RIVER NEAR THE MOUTH	3156	0
NRNFS	NATION RIVER NEAR FORT ST. JAMES	4942	0
NRNTM	NATION RIVER NEAR THE MOUTH	2549	0
ORAAC	OSPIKA RIVER ABOVE ALEY CREEK	2254	2
ORAOR	OMINECA RIVER ABOVE OSILINKA RIVER	6041	5
ORNEL	OSLINKA RIVER NEAR END LAKE	1868	1
PCRBH	POUCE COUPE RIVER BELOW HENDERSON CREEK	3256	0
PERNT	PEACE RIVER NEAR TAYLOR	5898	0
PRABD	PEACE RIVER AT BENNETT DAM	22878	<1
PRAEP	PINE RIVER AT EAST PINE	3756	0
PRAMR	PARSNIP RIVER ABOVE MISINCHINKA RIVER	4870	4
PRAOO	PACK RIVER AT OUTLET OF MCLEOD LAKE	4179	0
PRAPR	PEACE RIVER AT PEACE RIVER, AB	19306	0
RRNRG	REDWILLOW RIVER NEAR RIO GRANDE, AB	1310	0
SMRAW	SMOKY RIVER AT WATINO, AB	29700	0
SRNTM	SUKUNKA RIVER NEAR THE MOUTH	2849	<1
WRNGP	WAPITI RIVER NEAR GRANDE PRAIRIE, AB	10365	0
WRNTM	WASKAHIGAN RIVER NEAR THE MOUTH, AB	1154	0
TOTAL		203947	262

§ Glacier area c. 2000

Table A2. Fraser River sub-basins for the VICGL model

Basin Code	Sub-basin Name	Area (km^2)	Glacier Area (km^2)§
ADAMS	ADAMS RIVER NEAR SQUILAX	3130	46
BAKER	BAKER CREEK AT QUESNEL	1546	0
BARRM	BARRIERE RIVER AT THE MOUTH	1178	0
BCHAL	ALOUETTE RIVER AT ALOUETTE DAM	283	0
BCHLJ	BRIDGE RIVER AT LA JOIE DAM	946	173
BCHSF	STAVE RIVER AT STAVE FALLS DAM	942	0
BCHSG	SHUSWAP RIVER AT SUGAR DAM	1352	24
BCHST	SETON RIVER AT SETON DAM	890	8
BCHTR	BRIDGE RIVER AT TERZAGHI DAM	2745	67
BCHWL	SHUSWAP RIVER AT WILSEY DAM	1021	0
BIGCR	BIG CREEK ABOVE GROUNDHOG CREEK	997	10
BONAP	BONAPARTE RIVER BELOW CACHE CREEK	5334	0
BOWRB	BOWRON RIVER BELOW BOX CANYON	3364	0
CAYOO	CAYOOSH CREEK NEAR LILLOOET	954	3
CHILB	CHILCOTIN RIVER BELOW BIG CREEK	12254	0
CHILK	CHILKO RIVER NEAR REDSTONE	5385	331
CHILLI	CHILLIWACK RIVER AT VEDDER CROSSING	1713	0
CLEAO	CLEARWATER RIVER AT OUTLET OF CLEARWATER LAKE	3031	249
CLEAS	CLEARWATER RIVER NEAR CLEARWATER STATION	2585	0
COTTO	COTTONWOOD RIVER NEAR CINEMA	2150	<1
EAGLE	EAGLE RIVER NEAR MALAKWA	1033	68
FRSHA	FRASER RIVER AT HANSARD	7986	45
FRSHP	FRASER RIVER AT HOPE	31557	70
FRSMC	FRASER RIVER AT MCBRIDE	5487	422
FRSMG	FRASER RIVER NEAR MARGUERITE	20810	0
FRSMT	FRASER RIVER AT THE MOUTH	5989	154
FRSRP	FRASER RIVER AT RED PASS	2538	79
HARRI	HARRISON RIVER NEAR HARRISON HOT SPRINGS	6154	335
HORSE	HORSEFLY RIVER ABOVE MCKINLEY CREEK	1242	0
LILLO	LILLOOET RIVER NEAR PEMBERTON	2486	652
MAHOO	MAHOOD RIVER AT OUTLET OF MAHOOD LAKE	5078	0
MCGRE	MCGREGOR RIVER AT LOWER CANYON	5484	234
NAUTL	NAUTLEY RIVER NEAR FORT FRASER	3163	0
NAZKO	NAZKO RIVER ABOVE MICHELLE CREEK	3259	0
NECHC	NECHAKO RIVER BELOW CHESLATTA FALLS	16800	244
NICOL	NICOLA RIVER NEAR SPENCES BRIDGE	7747	0
NTHMB	NORTH THOMPSON RIVER AT BIRCH ISLAND	5066	310
QUESL	QUESNEL RIVER AT LIKELY	4702	118
QUESQ	QUESNEL RIVER NEAR QUESNEL	5551	91

Basin Code	Sub-basin Name	Area (km^2)	Glacier Area (km^2)§
SALMO	SALMON RIVER NEAR PRINCE GEORGE	4912	0
SANJO	SAN JOSE RIVER ABOVE BORLAND CREEK	1642	0
SEYMO	SEYMOUR RIVER NEAR SEYMOUR ARM	1024	47
STELL	STELLAKO RIVER AT GLENANNAN	4600	0
STHOM	SOUTH THOMPSON RIVER AT CHASE	9678	0
STUAR	STUART RIVER NEAR FORT ST. JAMES	15920	12
TASEK	TASEKO RIVER AT OUTLET OF TASEKO LAKES	1789	214
WESTR	WEST ROAD RIVER NEAR CINEMA	9261	0
WILLO	WILLOW RIVER ABOVE HAY CREEK	2844	0
TOTAL			

§ Glacier area c. 2000

Table A3. Columbia River sub-basins for the VICGL model

Basin Code	Sub-basin Name	Area (km^2)	Glacier Area (km^2)
ALB	WILLAMETTE RIVER AT ALBANY, OR	6846	0
ANA	SNAKE RIVER NEAR ANATONE, WA	10647	0
ASHNO	ASHNOLA RIVER NEAR KEREMEOS, BC	1079	0
BEAVE	BEAVER RIVER NEAR THE MOUTH, BC	1150	73
BFE	KOOTENAI RIVER AT BONNERS FERRY, ID	9225	1
BIGI	BOISE RIVER AT GLENWOOD BRIDGE NEAR BOISE, ID	7562	0
BITDA	BITTERROOT RIVER NEAR DARBY, MT	2802	0
BON	COLUMBIA RIVER BELOW BONNEVILLE DAM, OR	28535	42
BRI	KOOTENAY RIVER AT BRILLIANT DAM, BC	10169	75
BRN	SNAKE RIVER AT BROWNLEE DAM INFLOW, ID	8874	0
BruneauR	BRUNEAU RIVER NEAR HOT SPRING, ID	7064	0
BULWA	BULL RIVER NEAR WARDNER	1565	1
CHL	CHELAN RIVER AT CHELAN, WA	2390	28
COWKO	COWLITZ RIVER NEAR KOSMOS, WA	2732	12
CRNIC	COLUMBIA RIVER AT NICHOLSON, BC	6784	131
DCD	DUNCAN RIVER AT DUNCAN DAM, BC	1903	112
DEX	MIDDLE FORK WILLAMETTE RIVER NEAR DEXTER, OR	2693	0
DONAL	COLUMBIA RIVER AT DONALD, BC	1628	103
DWR	NORTH FORK CLEARWATER RIVER AT DWORSHAK DAM, ID	6071	0
ELKFE	ELK RIVER AT FERNIE, BC	3212	7
FLAWE	MIDDLE FORK FLATHEAD RIVER NEAR WEST GLACIER, MT	3219	17
GCL	COLUMBIA RIVER AT GRAND COULEE, WA	16891	0
GRANB	GRANBY RIVER AT GRAND FORKS, BC	2046	0
HANGM	HANGMAN CREEK AT SPOKANE, WA	1641	0
ILLEC	ILLECILLEWAET RIVER AT GREELEY, BC	1185	55
JDA	COLUMBIA RIVER AT JOHN DAY DAM, WA	38137	0
JFFO	SANTIAM RIVER AUX NEAR JEFFERSON, OR	4894	<1
JOECA	ST JOE RIVER AT CALDER, ID	2764	0
JOHND	JOHN DAY RIVER AT MCDONALD FERRY, OR	18694	0
KER	FLATHEAD RIVER AT KERR DAM, MT	15365	12
KETFE	KETTLE RIVER NEAR FERRY, WA	5885	0
KICHO	KICKING HORSE RIVER AT GOLDEN, BC	1726	46
KIMI	SNAKE RIVER NEAR KIMBERLY, ID	28120	0
KIOW	YAKIMA RIVER AT KIONA, WA	10499	<1
KOOTE	KOOTENAY RIVER AT FORT STEELE, BC	12006	37
LARMA	LARDEAU RIVER AT MARBLEHEAD, BC	1541	13
LIB	KOOTENAI RIVER AT LIBBY DAM, MT	6990	0
LIM	SNAKE RIVER BELOW MCDUFF RAPIDS (LIME POINT), ID	6925	0
LLK	SPOKANE RIVER AT LONG LAKE, WA	10741	0

Basin Code	Sub-basin Name	Area (km^2)	Glacier Area (km^2)
LORI	SNAKE RIVER AT LORENZO, ID	15287	5
Malheur	MALHEUR RIVER BELOW NEVADA DAM NEAR VALE, OR	9919	0
MAY	COWLITZ RIVER BELOW MAYFIELD DAM, WA	932	0
MCD	COLUMBIA RIVER AT MICA DAM, BC	10356	838
MER	LEWIS RIVER AT AERIAL (MERWIN), WA	1779	3
METPA	METHOW RIVER NEAR PATEROS, WA	4556	0
MISSI	MISSION CREEK NEAR EAST KELOWNA, BC	812	0
MUC	COLUMBIA RIVER AT MURPHY CREEK, BC	9968	126
OKA	OKANAGAN RIVER NEAR OLIVER, BC	1515	0
OKAPE	OKANAGAN RIVER AT PENTICTON, BC	5765	0
ORO	CLEARWATER RIVER AT OROFINO, ID	14367	0
OUTLET	COLUMBIA RIVER AT TIDEWATER, WA	10309	8
PLEI	PAYETTE RIVER NEAR LEATHA, ID	7550	0
PRD	COLUMBIA RIVER BELOW PRIEST RAPIDS DAM, WA	28145	2
PRVO	CROOKED RIVER NEAR PRINEVILLE, OR	5774	0
REXI	HENRYS FORK NEAR REXBURG, ID	8030	1
RML	CLACKAMAS RIVER AT ESTACADA (RIVER MILL), OR	2051	0
ROMO	OWYHEE RIVER NEAR ROME, OR	30251	0
RVC	COLUMBIA RIVER AT REVELSTOKE DAM, BC	5113	244
SIMHE	SIMILKAMEEN RIVER NEAR HEDLEY, BC	2356	0
SIMNI	SIMILKAMEEN RIVER NEAR NIGHTHAWK, WA	2221	0
SIMPR	SIMILKAMEEN RIVER AT PRINCETON, BC	1904	<1
SKHI	SNAKE RIVER AT KING HILL, ID	21825	0
SLOCR	SLOCAN RIVER NEAR CRESCENT VALLEY, BC	3250	2
SPD	CLEARWATER RIVER AT SPALDING, ID	2994	0
SVN	WILLAMETTE RIVER AT OREGON CITY (T.W. SULLIVAN), OR	8909	0
SWAI	SNAKE RIVER NEAR MURPHY, ID	10064	0
THOMP	THOMPSON RIVER NEAR THOMPSON FALLS, MT	1463	0
TOM	CLARK FORK NEAR PLAINS (THOMPSON FALLS DAM), MT	31659	1
TULPR	TULAMEEN RIVER AT PRINCETON, BC	2167	0
UMATI	UMATILLA RIVER NEAR UMATILLA, OR	6370	0
UMTW	YAKIMA RIVER AT UMTANUM, WA	4410	1
WARMS	WARM SPRINGS RIVER NEAR KAHNEETA HOT SPRINGS, OR	1403	0
WAT	PEND D'OREILLE RIVER AT WANETA DAM, BC	13706	0
WAV	MCKENZIE RIVER NEAR WALTERVILLE, OR	2848	3
WEII	SNAKE RIVER NEAR WEISER, ID	15387	0
WENPE	WENATCHEE RIVER AT PESHASTIN, WA	2570	7
WHB	SALMON RIVER AT WHITE BIRD, ID	35052	0
TOTAL		655238	2004

Table A4. Description of Manual Snow Survey (MSS) stations used in model validation and comparison of 1971-2000 April 1 SWE and elevation of corresponding VIC-GL model grid and elevation band. Values for each station include observed SWE (OBS_SWE; mm), simulated SWE (SIM_SWE; mm), the relative difference between simulated and observed SWE ((SIM-OBS)/OBS), station elevation (Z_STN; m), band elevation (Z_BAND; m) and elevation difference (Z_DIFF; m).

ID	STATION NAME	Longitude	Latitude	Z_STN	OBS_SWE	SIM_SWE	RDIFF_SWE	Z_BAND	Z_DIFF
1A01	YELLOWHEAD	-118.54632	52.90595	1860	507	276	-0.456	1858	-2
1A02	MCBRIDE (UPPER)	-120.32194	53.30500	1590	429	288	-0.329	1530	-60
1A03	BARKERVILLE	-121.49182	53.05734	1520	360	363	0.007	1510	-10
1A05	LONGWORTH (UPPER)	-121.44055	53.96583	1693	773	560	-0.275	1663	-31
1A06	HANSARD	-121.86557	54.08561	590	279	135	-0.515	644	54
1A06A	HANSARD	-121.86416	54.06778	622	204	135	-0.335	644	22
1A07	FORT ST.JAMES	-124.16115	54.48878	810	130	150	0.161	810	0
1A08	BOWRON LAKE	-121.37071	53.24975	1280	219	294	0.338	1277	-3
1A09	TORPY RIVER	-121.66995	54.08832	1070	435	362	-0.167	1094	24
1A10	PRINCE GEORGE AIRPORT	-122.67778	53.88111	684	118	105	-0.115	676	-8
1A11	PACIFIC LAKE	-121.57611	54.37278	756	628	279	-0.556	785	29
1A12	KAZA LAKE	-126.28805	56.01695	1247	341	247	-0.276	1259	12
1A13	LONGWORTH (LOWER)	-121.45668	53.94789	1230	292	348	0.189	1298	68
1A14	HEDRICK LAKE	-121.00000	54.10167	1113	688	359	-0.478	1116	3
1A15	KNUDSEN LAKE	-120.77944	54.30500	1598	826	589	-0.287	1525	-73
1A16	BURNS LAKE	-125.74555	54.23722	820	127	94	-0.262	846	26
1A17	REVOLUTION CREEK	-120.37420	53.78335	1690	855	612	-0.284	1666	-24
1A18	HOLMES RIVER	-119.46424	53.27879	1900	724	577	-0.203	1893	-7
1A19	DOME MOUNTAIN	-121.02440	53.62208	1766	761	523	-0.313	1700	-66
1A20	MCBRIDE (MIDDLE)	-120.30525	53.37161	1160	344	133	-0.613	1083	-77
1A21	NARROW LAKE	-121.89890	53.58143	1650	897	501	-0.441	1646	-4
1A22	MCBRIDE (LOWER)	-120.27851	53.33623	790	92	39	-0.582	744	-46
1A23	BIRD CREEK	-125.33889	53.67778	1196	152	98	-0.353	1235	39
1B01	MOUNT WELLS	-126.42361	53.72861	1489	524	285	-0.455	1496	7
1B02	TAHTSA LAKE	-127.66083	53.59306	1319	1179	722	-0.388	1267	-52

ID	STATION NAME	Longitude	Latitude	Z_STN	OBS_SWE	SIM_SWE	RDIFF_SWE	Z_BAND	Z_DIFF
1B05	SKINS LAKE	-125.99972	53.77945	877	111	78	-0.300	866	-12
1B06	MOUNT SWANNELL	-125.27111	53.35584	1596	308	222	-0.281	1649	53
1C01	BROOKMERE	-120.88111	49.81333	994	201	46	-0.770	947	-47
1C02	PORCUPINE RIDGE	-120.59354	51.02049	1830	424	138	-0.674	1650	-180
1C03	TRANQUILLE LAKE	-120.59755	50.93593	1420	224	128	-0.428	1369	-51
1C04	PASS LAKE	-120.50480	50.84894	870	53	5	-0.900	912	42
1C05	MCGILLIVRAY PASS	-122.62694	50.69472	1715	602	342	-0.432	1697	-18
1C07	LAC LE JEUNE (LOWER)	-120.59291	50.68004	1370	97	177	0.822	1441	71
1C08	NAZKO	-123.66083	53.01695	1029	64	103	0.610	1078	49
1C09A	HIGHLAND VALLEY	-120.98330	50.50000	1457	96	53	-0.451	1483	26
1C10	FRENCH SNOWSHOE	-121.49096	52.79986	1580	674	292	-0.567	1434	-146
1C12	GREEN MOUNTAIN	-122.88393	50.77688	1630	662	425	-0.358	1680	50
1C13	BLACK MOUNTAIN	-121.17321	52.33213	1570	499	530	0.062	1622	52
1C13A	HORSEFLY MOUNTAIN	-121.05083	52.33889	1612	464	263	-0.433	1504	-108
1C14	BRALORNE	-122.79638	50.77945	1382	178	114	-0.360	1315	-67
1C17	MOUNT TIMOTHY	-121.25416	51.91500	1632	327	342	0.046	1628	-4
1C19	GNAWED MOUNTAIN	-120.96670	50.43330	1617	125	33	-0.736	1583	-34
1C20	BOSS MTN. MINE	-120.88490	52.14760	1500	584	335	-0.426	1450	-50
1C21	BIG CREEK	-123.03389	51.72861	1130	16	73	3.478	1140	10
1C22	PUNTZI MOUNTAIN	-124.08472	52.11861	939	31	10	-0.688	917	-22
1C23	PENFOLD CREEK	-120.55916	52.74556	1687	1009	1119	0.108	1740	53
1C24	YANKS PEAK	-121.41481	52.85050	1710	772	506	-0.345	1700	-10
1C25	LAC LE JEUNE (UPPER)	-120.49138	50.45750	1471	127	56	-0.561	1493	22
1C28	DUFFEY LAKE	-122.47444	50.37278	1253	480	342	-0.288	1311	58
1C29	SHOVELNOSE MOUNTAIN	-120.86416	49.86417	1456	240	279	0.163	1469	13
1C30	SPAHOMIN	-120.35865	50.12526	1450	72	165	1.304	1447	-3
1C31	CONANT LAKE	-120.53617	50.36252	1370	188	25	-0.867	1361	-9
1C32	DEADMAN RIVER	-120.61670	51.10000	1463	104	115	0.102	1466	3
1D06	TENQUILLE LAKE	-122.92874	50.53544	1680	1159	849	-0.268	1737	57

ID	STATION NAME	Longitude	Latitude	Z_STN	OBS_SWE	SIM_SWE	RDIFF_SWE	Z_BAND	Z_DIFF
1D08	STAVE LAKE	-122.30500	49.57611	1211	1554	1805	0.162	1298	87
1D10	NAHATLATCH RIVER	-122.05083	49.83028	1530	1417	1191	-0.159	1518	-12
1D11	BOSTON BAR CREEK (UPPER)	-121.21624	49.58467	1340	1171	952	-0.187	1301	-39
1D12	BOSTON BAR CREEK (LOWER)	-121.10249	49.59429	1230	740	769	0.039	1303	73
1D14	OTTOMITE	-121.15365	49.60276	1460	1293	1101	-0.149	1488	28
1D15	GREAT BEAR	-121.10710	49.48604	1660	1321	1073	-0.187	1679	19
1E01A	BLUE RIVER TOWN	-119.27065	52.11968	670	284	179	-0.370	685	15
1E01B	BLUE RIVER	-119.28805	52.11861	673	272	179	-0.342	685	12
1E02A	MOUNT COOK	-119.43683	52.21132	1580	1252	525	-0.580	1511	-69
1E03A	TROPHY MOUNTAIN	-119.94889	51.81333	1907	548	531	-0.030	1849	-58
1E04	MOUNT ALBREDA	-119.04840	52.49949	1920	740	692	-0.065	1899	-21
1E05	KNOUFF LAKE	-120.13330	50.98330	1189	144	120	-0.164	1132	-57
1E06	COOK FORKS	-119.47990	52.17278	1390	897	409	-0.544	1342	-48
1E07	ADAMS RIVER	-119.42361	51.59306	1769	707	478	-0.324	1725	-44
1E08	AZURE RIVER	-119.69101	52.66853	1620	1086	646	-0.405	1709	89
1E12	MCQUEEN LAKE	-120.39534	50.79462	1100	69	90	0.318	1048	-52
1F01A	ABERDEEN LAKE	-119.05083	50.13556	1262	143	210	0.472	1294	32
1F01B	HADDO LAKE	-119.11051	50.07375	1300	116	184	0.580	1304	4
1F02	ANGLEMONT	-119.18638	50.99972	1168	353	359	0.018	1112	-56
1F03	PARK MOUNTAIN	-118.61652	50.44690	1890	911	593	-0.349	1858	-32
1F04	ENDERBY	-118.93194	50.66083	1948	1019	726	-0.287	1889	-59

Table A5. Peace basin calibration and validation performance by sub-basin

Basin	KGE_Q		LNSE_Q		HMLE_Q[‡]		BMF_ET		KGE_SCA		BMF_B	
	calib	valid	calib	valid	calib	valid	calib	valid	calib	valid	calib	valid
ARNT7	0.73	0.75	0.88	0.87	2.27	2.13	0.48	0.46	0.79	0.84	0.97	0.81
BRBAC	0.21	0.18	0.18	0.13	10.14	7.83	0.48	0.41	0.90	0.96		
BRNFS	0.57	0.59	0.47	0.41	51.18	38.90	0.52	0.42	0.86	0.92		
FRAAR	0.91	0.87	0.78	0.77	25.46	25.51	0.46	0.42	0.80	0.82	0.98	0.58
GRACC	0.78	0.80	0.82	0.77	2.11	2.93	0.43	0.43	0.83	0.83		
HERNN	0.48	0.43	0.20	0.03	3.18	3.12	0.57	0.58	0.88	0.95		
HRAGR	0.59		0.72		6.89		0.46		0.78			
HRNFC	0.76	0.53	0.96	0.72	0.88	10.03	0.48	0.46	0.93	0.95		
IRASR	0.86	0.84	0.19	0.44	12.13	9.13	0.52	0.48	0.78	0.80		
KIRNF	0.49	0.17	0.09	0.00	>1000	11.10	0.43	0.44	0.91	0.95		
KWRNW	0.91		0.67		4.13		0.50		0.86		0.95	
LSRNG	0.39	0.45	0.38	0.21	48.29	41.79	0.50	0.54	0.77	0.95		
MRAGC	0.89	0.84	0.89	0.91	2.42	2.06	0.53	0.49	0.83	0.86		
MRAWR	0.80	0.77	0.75	0.75	11.07	9.16	0.43	0.43	0.80	0.82	1.00	0.97
MRNFS	0.87	0.81	0.56	0.77	1.94	1.31	0.54	0.57	0.79	0.84		
MRNTM	0.96	0.72	0.96	0.80	1.36	10.13	0.51	0.55	0.83	0.84		
NRNFS	0.96		0.90		2.09		0.53		0.85			
NRNTM	0.98	0.80	0.98	0.84	0.37	3.08	0.40	0.45	0.80	0.79		
ORAAC	0.90	0.85	0.43	0.39	5.26	4.17	0.45	0.48	0.85	0.85		
ORAOR	0.93	0.86	0.73	0.75	6.01	3.78	0.59	0.55	0.85	0.86	0.74	0.19
ORNEL	0.92	0.89	0.85	0.87	2.31	1.51	0.54	0.54	0.82	0.84		
PCRBH	0.41	0.36	-0.03	-0.21	13.56	17.45	0.53	0.48	0.81	0.96		
PERNT[§]	0.99		0.96		11.00		0.53		0.84			
PRABD[§]	0.97	0.92	0.97	0.90	8.97	36.25	0.49	0.51	0.85	0.85		
PRAEP	0.96	0.80	0.98	0.85	1.13	11.06	0.49	0.52	0.81	0.83		
PRAMR	0.73	0.78	0.19	0.38	49.15	36.38	0.41	0.47	0.73	0.76	0.88	0.16
PRAOO	0.87	0.82	0.71	0.73	3.11	2.87	0.41	0.42	0.83	0.86		

Basin	KGE_Q		LNSE_Q		HMLE_Q‡		BMF_ET		KGE_SCA		BMF_B	
	calib	valid	calib	valid	calib	valid	calib	valid	calib	valid	calib	valid
PRAPR§	0.99		0.99		9.52		0.71		0.86			
RRNRG	0.47	0.29	0.12	-0.12	>1000	>1000	0.54	0.53	0.89	0.96		
SMRAW	0.93	0.76	0.94	0.71	8.06	43.78	0.67	0.63	0.88	0.95	0.97	0.73
SRNTM	0.88	0.82	0.79	0.81	4.62	3.23	0.39	0.45	0.80	0.80		
WRNGP	0.78	0.72	0.72	0.59	11.84	21.22	0.68	0.68	0.89	0.91	1.00	0.76
WRNTM	0.41	0.31	0.02	0.00	>1000	>1000	0.51	0.54	0.78	0.96		

‡ Value show has been normalized by the mean observed flow

§ Calibration based on naturalized discharge

Table A6. Fraser basin calibration and validation performance by sub-basin

Basin	KGE_Q		LNSE_Q		HMLE_Q[‡]		BMF_ET		KGE_SCA		BMF_B	
	calib	valid	calib	valid	calib	valid	calib	valid	calib	valid	calib	valid
ADAMS	0.90	0.90	0.75	0.77	3.76	4.31	0.48	0.55	0.82	0.86	0.65	0.54
BAKER	0.81	0.65	0.38	0.28	1.18	1.11	0.56	0.58	0.76	0.75		
BARRM	0.95	0.95	0.91	0.88	0.44	0.44	0.63	0.66	0.81	0.86		
BCHAL[§]	0.70	0.37	0.61	0.66	4.23	2.07	0.41	0.42	0.75	0.78		
BCHLJ[§]	0.77	0.90	0.61	0.86	3.00	1.65	0.38	0.40	0.95	0.92	0.95	0.93
BCHSF[§]	0.61	0.56	0.72	0.71	16.81	16.48	0.50	0.57	0.85	0.85	0.93	0.00
BCHSG[§]	0.80	0.81	-0.56	-0.41	6.13	4.30	0.41	0.39	0.89	0.93	1.00	0.99
BCHST[§]	0.81	0.61	0.68	0.65	2.65	2.13	0.46	0.31	0.79	0.84	0.63	0.84
BCHTR[§]	0.81	0.03	0.81	0.46	3.98	25.03	0.42	0.43	0.93	0.95	0.04	0.48
BIGCR	0.67	0.76	0.76	0.81	0.91	0.52	0.41	0.42	0.85	0.81	0.12	0.96
BONAP	0.83	0.66	0.78	0.62	0.59	0.92	0.62	0.57	0.89	0.75		
BOWRB	0.86	0.85	0.32	0.41	6.18	5.09	0.59	0.56	0.76	0.81		
CAYOO[§]	0.84	0.79	0.65	0.61	1.92	2.28	0.38	0.32	0.80	0.85	0.66	0.55
CHILB	0.98	0.27	0.96	0.82	1.66	9.23	0.71	0.71	0.82	0.75		
CHILK	0.92	0.31	0.91	0.81	2.39	5.53	0.53	0.53	0.87	0.85	0.74	0.73
CHILLI	0.80	0.81	0.41	0.59	7.55	6.35	0.37	0.40	0.95	0.96		
CLEAO	0.89	0.85	0.25	0.27	8.44	12.14	0.40	0.40	0.82	0.86	1.00	0.46
CLEAS	0.96	0.90	0.96	0.64	3.60	14.22	0.50	0.52	0.74	0.85		
EAGLE	0.88	0.88	0.10	0.15	3.68	3.19	0.42	0.44	0.91	0.93	0.91	1.00
FRSHA	0.92	0.76	0.88	0.63	15.93	34.55	0.49	0.41	0.85	0.88	1.00	0.64
FRSHP[§]	0.99	0.89	0.99	0.87	11.97	80.25	0.69	0.69	0.72	0.71	0.24	0.90
FRSMC	0.89	0.52	0.86	0.85	6.39	10.08	0.43	0.40	0.83	0.87	1.00	0.44
FRSMG[§]	0.98	0.85	0.97	0.75	13.17	81.19	0.50	0.63	0.81	0.82		
FRSRP	0.67	0.50	-0.15	-0.09	5.31	7.31	0.43	0.37	0.93	0.95	0.48	0.73
HARRI	0.84	0.73	0.79	0.68	16.45	26.81	0.44	0.41	0.84	0.89	0.88	0.62
HORSE	0.88	0.89	0.74	0.83	1.20	1.00	0.64	0.66	0.83	0.86		
LILLO	0.84	0.89	0.82	0.83	9.30	6.85	0.48	0.46	0.84	0.82	0.79	0.75

Basin	KGE_Q		LNSE_Q		HMLE_Q[‡]		BMF_ET		KGE_SCA		BMF_B	
	calib	valid	calib	valid	calib	valid	calib	valid	calib	valid	calib	valid
MAHOO	0.76	0.83	0.44	0.71	12.17	5.95	0.53	0.64	0.69	0.75		
MCGRE	0.83	0.83	0.78	0.74	15.01	17.08	0.46	0.46	0.83	0.86	0.88	0.48
NAUTL	0.92	0.67	0.94	0.71	0.82	2.45	0.53	0.58	0.89	0.84		
NECHC[§]	0.91	0.79	0.69	0.40	17.02	24.64	0.60	0.66	0.88	0.88	0.19	0.58
NICOL	0.90	0.80	0.80	0.74	1.98	1.94	0.50	0.53	0.87	0.87		
NTHMB	0.88	0.86	0.86	0.79	8.97	11.81	0.47	0.50	0.88	0.92	1.00	0.49
QUESL	0.96	0.91	0.92	0.81	3.93	7.57	0.58	0.67	0.79	0.82	0.99	0.64
QUESQ	0.93	0.91	0.92	0.86	5.24	9.31	0.57	0.58	0.85	0.88	1.00	0.53
SALMO	0.80	0.74	-0.08	-0.03	5.99	3.93	0.52	0.55	0.82	0.83		
SANJO	0.70	0.44	0.57	-0.08	0.40	0.49	0.53	0.58	0.85	0.77		
SEYMO	0.83	0.83	0.21	0.31	3.67	3.05	0.37	0.37	0.93	0.96	1.00	0.42
STELL	0.90	0.70	0.77	0.70	1.87	2.56	0.62	0.69	0.87	0.87		
STHOM	0.95	0.94	0.96	0.83	3.54	11.88	0.67	0.68	0.84	0.88		
STUAR	0.95	0.92	0.88	0.88	5.18	3.80	0.59	0.62	0.84	0.83	0.22	0.99
TASEK	0.74	-0.24	0.83	0.74	1.88	4.24	0.38	0.19	0.86	0.83	0.99	0.89
WESTR	0.91	0.61	0.63	0.23	2.80	4.20	0.55	0.60	0.86	0.76		
WILLO	0.88	0.85	0.66	0.57	3.44	4.95	0.55	0.50	0.74	0.82		

‡ Value show has been normalized by the mean observed flow

§ Calibration based on naturalized discharge

Table A7. Columbia basin calibration and validation performance by sub-basin

Basin	KGE_Q		LNSE_Q		HMLE_Q‡		BMF_ET		KGE_SCA		BMF_B	
	calib	valid	calib	valid	calib	valid	calib	valid	calib	valid	calib	valid
ALB§	0.96	0.88	0.97	0.82	5.03	27.47	0.48	0.49	-0.86	-0.32		
ANA§	1.00	0.81	0.99	0.81	1.82	48.60	0.45	0.44	0.50	0.60		
ASHNO	0.79	0.76	0.85	0.78	0.58	0.98	0.38	0.40	0.84	0.88		
BEAVE	0.86	0.70	0.84	0.78	2.77	3.20	0.36	0.35	0.88	0.91	1.00	0.98
BFE§	0.98	0.91	0.94	0.86	6.66	19.86	0.41	0.51	0.68	0.72		
BIGI§	0.86	0.84	0.78	0.70	8.39	7.65	0.29	0.32	0.80	0.89		
BITDA	0.89	0.67	0.84	0.76	1.29	1.44	0.40	0.43	0.87	0.87		
BON§	0.98	0.93	1.00	0.86	6.45	163.50	0.21	0.18	0.89	0.46		
BRI§	0.91	0.87	0.95	0.89	13.19	28.57	0.45	0.44	0.79	0.82	0.93	0.61
BRN§	0.99	0.70	1.00	0.63	0.59	49.12	0.30	0.37	0.69	0.65		
BruneauR§	0.89	0.83	0.81	0.75	0.89	0.97	0.55	0.56	0.53	0.78		
BULWA§	0.87	0.83	0.85	0.85	1.59	1.72	0.54	0.60	0.82	0.87		
CHL§	0.78	0.79	0.73	0.67	7.58	8.53	0.27	0.27	0.86	0.89		
COWKO	0.81	0.73	0.15	0.15	18.86	23.53	0.40	0.47	0.44	0.56		
CRNIC	0.94	0.84	0.86	0.88	5.61	4.45	0.41	0.40	0.87	0.88	0.98	0.95
DCD§	0.87	0.85	0.86	0.84	8.07	7.58	0.47	0.54	0.86	0.86	1.00	0.76
DEX§	0.87	0.75	-4.72	-5.90	14.62	24.24	0.50	0.44	0.61	0.73		
DONAL	0.93	0.75	0.98	0.91	1.13	7.09	0.45	0.40	0.90	0.91	0.93	0.99
DWR§	0.82	0.80	0.35	0.23	35.55	29.89	0.41	0.41	0.73	0.73		
ELKFE	0.83	0.92	0.87	0.84	2.09	2.59	0.53	0.49	0.81	0.83	0.21	1.00
FLAWE	0.90	0.78	0.80	0.76	6.14	7.07	0.52	0.56	0.91	0.92		
GCL§	1.00	0.93	1.00	0.89	2.01	96.01	0.46	0.45	0.80	0.82		
GRANB	0.94	0.85	0.32	0.40	3.52	6.07	0.49	0.55	0.77	0.85		
HANGM	0.35	0.32	0.25	0.18	>1000	>1000	0.30	0.25	-0.06	-0.46		
ILLEC	0.86	0.82	0.89	0.90	1.65	1.56	0.37	0.39	0.90	0.92	0.94	0.96
JDA§	0.99	0.92	1.00	0.87	3.24	165.04	0.46	0.46	-1.85	-1.34		
JFFO	0.87	0.85	-0.68	-0.71	34.54	25.79	0.40	0.32	0.01	0.20		

Basin	KGE_Q		LNSE_Q		HMLE_Q‡		BMF_ET		KGE_SCA		BMF_B	
	calib	valid	calib	valid	calib	valid	calib	valid	calib	valid	calib	valid
JOECA	0.81	0.78	0.01	0.04	13.31	12.70	0.33	0.35	0.66	0.70		
JOHND	0.70	0.34	0.55	0.46	31.64	50.69	0.40	0.40	0.12	0.22		
KER§	0.92	0.88	0.90	0.83	12.10	14.17	0.69	0.74	0.85	0.88		
KETFE	0.94	0.83	0.84	0.69	2.87	6.47	0.52	0.59	0.80	0.86		
KICHO	0.88	0.56	0.92	0.86	0.93	2.62	0.53	0.50	0.84	0.85	0.97	0.75
KIMI§	0.98	0.73	0.95	0.78	4.36	18.60	0.57	0.62	0.77	0.78		
KIOW§	0.84	0.57	0.79	0.08	8.56	24.35	0.34	0.35	0.20	-0.13		
KOOTE	0.89	0.87	0.90	0.87	8.94	10.46	0.57	0.56	0.87	0.87	0.38	0.91
LARMA	0.83	0.82	0.87	0.82	1.69	2.18	0.52	0.62	0.86	0.87	1.00	0.92
LIB§	0.98	0.91	0.94	0.82	5.42	22.08	0.64	0.70	0.68	0.75		
LIM§	0.99	0.83	0.99	0.78	1.37	49.01	0.20	0.22	0.51	0.56		
LLK§	0.84	0.70	0.71	0.43	21.52	47.37	0.41	0.43	0.31	0.38		
LORI§	0.92	0.84	0.85	0.82	8.64	8.48	0.55	0.55	0.87	0.91		
Malheur§	0.48	-0.04	0.24	-0.86	8.97	>1000	0.31	0.44	0.66	0.59		
MAY§	0.96	0.77	0.95	0.20	2.62	41.67	0.34	0.36	-1.34	-0.31		
MCD§	0.95	0.86	0.94	0.92	14.00	22.06	0.48	0.46	0.92	0.94	0.96	0.70
MER§	0.79	0.83	0.72	0.67	21.32	23.77	0.32	0.31	0.27	0.40		
METPA	0.90	0.87	0.88	0.81	2.17	3.33	0.44	0.45	0.83	0.89		
MISSI§	0.92	0.84	0.84	0.76	0.46	0.61	0.61	0.61	0.86	0.88		
MUC§	0.95	0.87	0.97	0.90	24.44	63.37	0.60	0.71	0.85	0.89	0.97	0.97
OKA§	0.97		0.98		0.00	35.06	0.57		0.64			
OKAPE§	0.92		0.88		0.00	15.06	0.59		0.89			
ORO§	0.90	0.85	0.70	0.66	30.69	100.68	0.49	0.48	0.67	0.68		
PLEI§	0.90	0.76	0.71	0.65	>1000	3.99	0.46	0.51	0.76	0.81		
PRD§	1.00	0.94	1.00	0.89	0.61	8.25	0.36	0.34	0.25	0.08		
PRVO§	0.76		0.00		>1000	17.48	0.12		0.58			
REXI§	0.91	0.80	0.79	0.71	5.42	22.23	0.51	0.51	0.89	0.90		
RML§	0.62	0.71	0.69	0.69	9.76	4.04	0.33	0.31	0.30	0.27		

Basin	KGE_Q		LNSE_Q		HMLE_Q‡		BMF_ET		KGE_SCA		BMF_B	
	calib	valid	calib	valid	calib	valid	calib	valid	calib	valid	calib	valid
ROMO§	0.69	0.70	0.31	0.44	19.12	6.43	0.52	0.60	0.40	0.67		
RVC§	0.96	0.85	0.99	0.94	3.26	2.36	0.43	0.51	0.86	0.89	1.00	1.00
SIMHE	0.98	0.80	0.98	0.78	0.30	21.45	0.48	0.50	0.90	0.92		
SIMNI	0.98	0.81	0.97	0.75	0.83	1.92	0.47	0.48	0.71	0.78		
SIMPR	0.80	0.65	0.79	0.74	2.95	80.79	0.46	0.49	0.79	0.84		
SKHI§	0.92	0.65	0.92	0.56	3.76	38.55	0.46	0.44	0.67	0.74		
SLOCR	0.88	0.89	0.88	0.90	2.26	19.27	0.55	0.63	0.86	0.89		
SPD§	0.74	0.75	-0.30	0.64	115.90	0.74	0.29	0.27	-0.41	-0.37		
SVN§	0.98	0.88	0.95	0.82	14.77	22.82	0.43	0.41	-1.96	-1.28		
SWAI§	0.98	0.69	0.98	0.64	1.09	1.85	0.51	0.46	-1.26	-0.83		
THOMP	0.83	0.74	0.77	0.76	0.63	>1000	0.52	0.56	0.64	0.69		
TOM§	0.99	0.89	0.97	0.87	5.26	15.98	0.51	0.53	0.83	0.77		
TULPR	0.89	0.81	0.81	0.78	1.08	6.22	0.44	0.52	0.81	0.85		
UMATI	0.74	0.42	0.37	0.35	>1000	30.38	0.34	0.37	-0.86	-0.52		
UMTW§	0.72	0.61	0.25	0.13	12.66	21.75	0.36	0.38	0.55	0.57		
WARMS	0.56	-0.12	-0.37	-1.14	6.19	45.47	0.24	0.27	-0.09	-0.46		
WAT§	0.97	0.91	0.95	0.85	11.12	10.52	0.42	0.51	0.95	0.95		
WAV§	0.75	0.76	0.55	0.50	19.62	11.72	0.57	0.50	0.48	0.60		
WEII§	0.98	0.73	0.97	0.65	4.73	0.00	0.50	0.54	0.10	0.10		
WENPE	0.85	0.76	0.78	0.71	5.43	0.00	0.35	0.39	0.78	0.82		
WHB§	0.93	0.91	0.87	0.85	12.03	0.15	0.42	0.43	0.87	0.86		

‡ Value show has been normalized by the mean observed flow

§ Calibration based on naturalized discharge